A 3D-Printed Assemblable Bespoke Scaffold as a Versatile Microcryogel Carrier for Site-Specific Regenerative Medicine

Journal Article

Author(s):
Lee, Seunghun S.; Kleger, Nicole; Kuhn, Gisela A.; Greutert, Helen; Du, Xiaoyu (ID); Smit, Thijs; Studart, André R.; Ferguson, Stephen J. (ID)

A 3D-Printed Assemblable Bespoke Scaffold as a Versatile Microcryogel Carrier for Site-Specific Regenerative Medicine

Seunghun S. Lee,* Nicole Kleger, Gisela A. Kuhn, Helen Greutert, Xiaoyu Du, Thijs Smit, André R. Studart, and Stephen J. Ferguson

Advances in additive manufacturing have led to diverse patient-specific implant designs utilizing computed tomography, but this requires intensive work and financial implications. Here, Digital Light Processing is used to fabricate a hive-structured assemblable bespoke scaffold (HIVE). HIVE can be manually assembled in any shape/size with ease, so a surgeon can create a scaffold that will best fit a defect before implantation. Simultaneously, it can have site-specific treatments by working as a carrier filled with microcryogels (MC) incorporating different biological factors in different pockets of HIVE. After characterization, possible site-specific applications are investigated by utilizing HIVE as a versatile carrier with incorporated treatments such as growth factors (GF), bioceramic, or cells. HIVE as a GF-carrier shows a controlled release of bone morphogenetic protein/vascular endothelial growth factor (BMP/VEGF) and induced osteogenesis/angiogenesis from human mesenchymal stem cells (hMSC)/human umbilical vein endothelial cells (HUVECs). Furthermore, as a bioceramic-carrier, HIVE demonstrates enhanced mineralization and osteogenesis, and as a HUVEC carrier, it upregulates both osteogenic and angiogenic gene expression of hMSCs. HIVE with different combinations of MCs yields a distinct local effect and successful cell migration is confirmed within assembled HIVEs. Finally, an in vivo rat subcutaneous implantation demonstrates site-specific osteogenesis and angiogenesis.

S. S. Lee, G. A. Kuhn, H. Greutert, X. Du, T. Smit, S. J. Ferguson
Institute for Biomechanics
Department of Health Sciences and Technology
ETH Zurich
Zurich 8092, Switzerland
E-mail: seunglee@ethz.ch
N. Kleger, A. R. Studart
Complex Materials
Department of Materials
ETH Zurich
Zurich 8093, Switzerland

1. Introduction

The number of orthopedic-related fractures and injuries has increased with the exponential growth of the elderly population. Since bone is a complex tissue that continuously undergoes dynamic biological remodeling to maintain homeostasis, cutting-edge technology that can address these issues is required.[1] As a result, bone tissue engineering (BTE) has emerged as a solution with huge potential, and various 3D printing technologies have facilitated a substantial development in BTE scaffold design.[2] Especially, recent advances in addictive manufacturing have allowed to fabricate patient-specific scaffolds and implants based on computed tomography images of the patient, however, the process is labor-intensive and costly.[3] Moreover, it takes a substantial amount of time for patient-specific implants to be designed, 3D-printed, and delivered for surgery, which would create additional suffering and cost to patients. Particularly, it is not an optimal solution for patients in developing countries where there are problems such as limited medical facilities and a poor economic situation preventing access to advanced treatments.[4] Therefore, research to develop scaffolds that are affordable, easy to use, off-the-shelf, and can be adjusted to fit any size and shape of defect would be required to address these problems.[5] Furthermore, the scaffolds should be biocompatible and biomechanically stable under physiological loading and have multifunctional biological benefits, like angiogenesis and osteogenesis promotion to enhance tissue regeneration.[6]
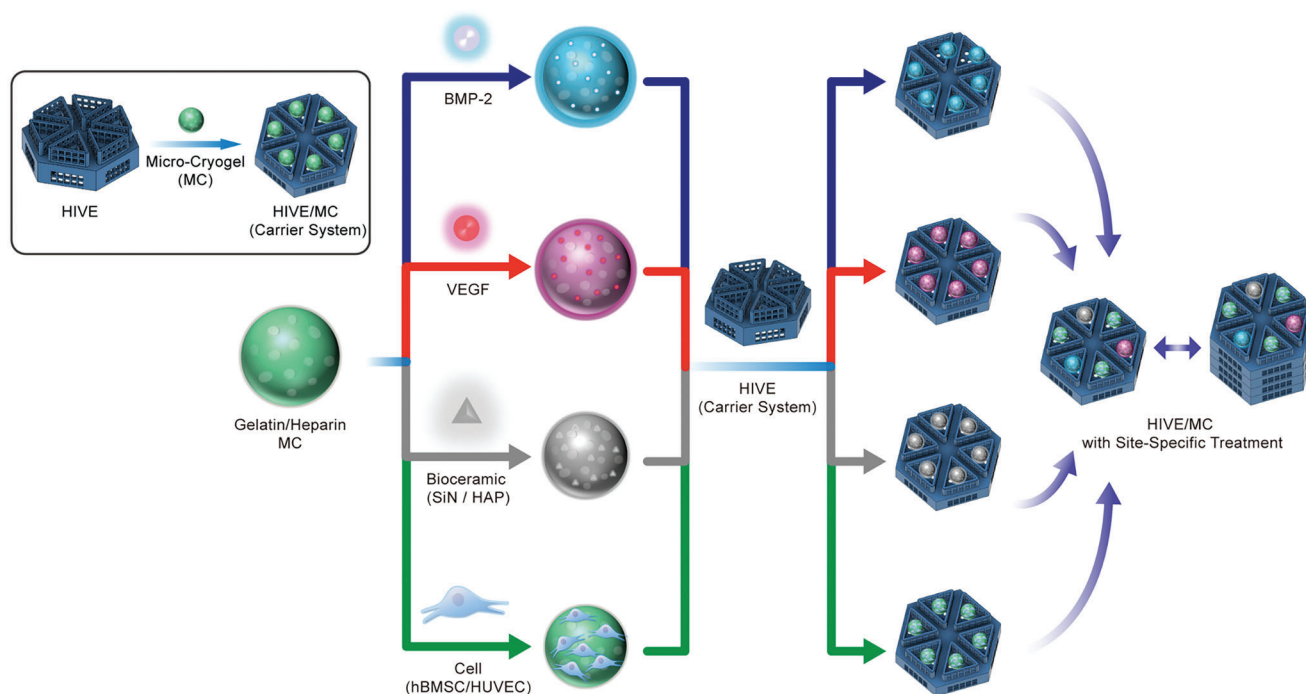
Here, we present the idea of a hive-structured assemblable bespoke scaffold (HIVE) system that can fulfill all these aims. We have used a Digital Light Processing (DLP) 3D-printing technique to fabricate the HIVE. The HIVE can be manually assembled in any shape or size with ease, much like the conventional plastic building toy Lego. This allows users to effortlessly scale up/down and assemble any arbitrary complex structure, which would help a surgeon to swiftly and intuitively create a scaffold that would fit the defect, immediately prior to implantation during the surgery, without any need for special instruments. Despite its excellent potential, in the field of regenerative medicine,

**ADVANCED
SCIENCE NEWS**

www.advancedsciencenews.com

**ADVANCED
MATERIALS**

www.advmat.de

Figure 1. Schematic illustration of hive-structured assemblable bespoke scaffold (HIVE) system with multifunctional MC. First, the empty HIVE scaffold was 3D printed by DLP, and gelatin/heparin MC was fabricated. Then, depending on the therapeutic aim, MC was loaded with GF such as BMP-2, VEGF, bioceramics, or cells. The prepared MCs were placed in designated pockets of HIVE for site-specific treatment. HIVE/MC could be used solely or be assembled with other HIVE/MC systems to fit the size of the defect or to enhance the therapeutic effect.

the evaluation of assemblable scaffolds has been relatively limited, with only a few studies conducted thus far.[7] For instance, Xia et al. demonstrated the assembly of PLGA-based microgels into microtissue through the utilization of a Michael addition reaction.[7b] Additionally, Subbiah et al. conducted studies of a lithography-based 3D-printed beta-tricalcium phosphate modular microcage scaffold with GelMA hydrogels containing growth factors (GF) like PDGF and VEGF.[7a] While these studies explored different approaches to enhance therapeutic outcomes, there is still a need for further research to develop an improved system with advanced functions, including multiple and site-specific effects. To address this gap, the HIVE system can provide site-specific treatments by serving as a carrier filled with micro-cryogels (MC) incorporating different biological factors, which have been developed in our previous studies,[1d,8] in each pocket of HIVE (**Figure 1**). Unlike conventional hydrogel-based scaffolds for cell or drug delivery, which have typically insufficient mechanical properties as a bone implant and poor localization,[9] the HIVE is designed to withstand physiological loading and be placed at an exact site for patient-specific treatment and biologic delivery. In this study, we investigated the potential of site-specific treatment by utilizing HIVE as a versatile carrier with incorporated cargo, such as GF (bone morphogenetic protein (BMP), vascular endothelial growth factor (VEGF)), bioceramic (silicon nitride (SiN), hydroxyapatite (HAP)) or cells (human mesenchymal stem cells (hMSC), human umbilical vein endothelial cells (HUVEC)). After characterization of the intrinsic HIVE properties, we analyzed various cellular responses with the HIVE as both a single biological factor carrier with different conditions and as a

mixed carrier, to evaluate biological effects such as osteogenesis and angiogenesis of hMSC and HUVEC and also cellular activity such as cell migration within HIVE assemblies. Finally, we checked the biological response and osteogenic/angiogenic effect of the HIVE in an in vivo rat subcutaneous implantation model.

2. Results

2.1. 3D Printing of Hive-Structured Assemblable Bespoke Scaffold (HIVE)

In order to enable pre-operative assembly and fitting to the defect, the HIVE is designed similarly to conventional interlocking toy blocks. However, the main exoskeleton design of the scaffold is based on a hexagon shape which is known to be one of the most space-efficient and mechanically strong shapes. With the main hexagon exoskeleton, the scaffold is divided into 6 triangular pockets that can serve as carriers for an MC and also ensure the interlocking fixation between scaffolds during assembly. Furthermore, we designed the overall structure and walls of the pockets in HIVE to incorporate macropores (500 × 500 µm-size square-shaped pores and Ø 500 µm-size circular-shaped pores) to allow cell migration for faster tissue regeneration. The HIVE scaffolds were 3D printed by a DLP technique, with nominal dimensions of 10 mm × 11.5 mm × 4 mm per unit, 167–567 µm-thick struts, and porosity of 72% as shown in **Figure 2**a. After 3D printing, the scaffolds were examined by light microscopy and field-emission scanning electron microscopy (SEM) to check the printing quality. All samples were well fabricated, without
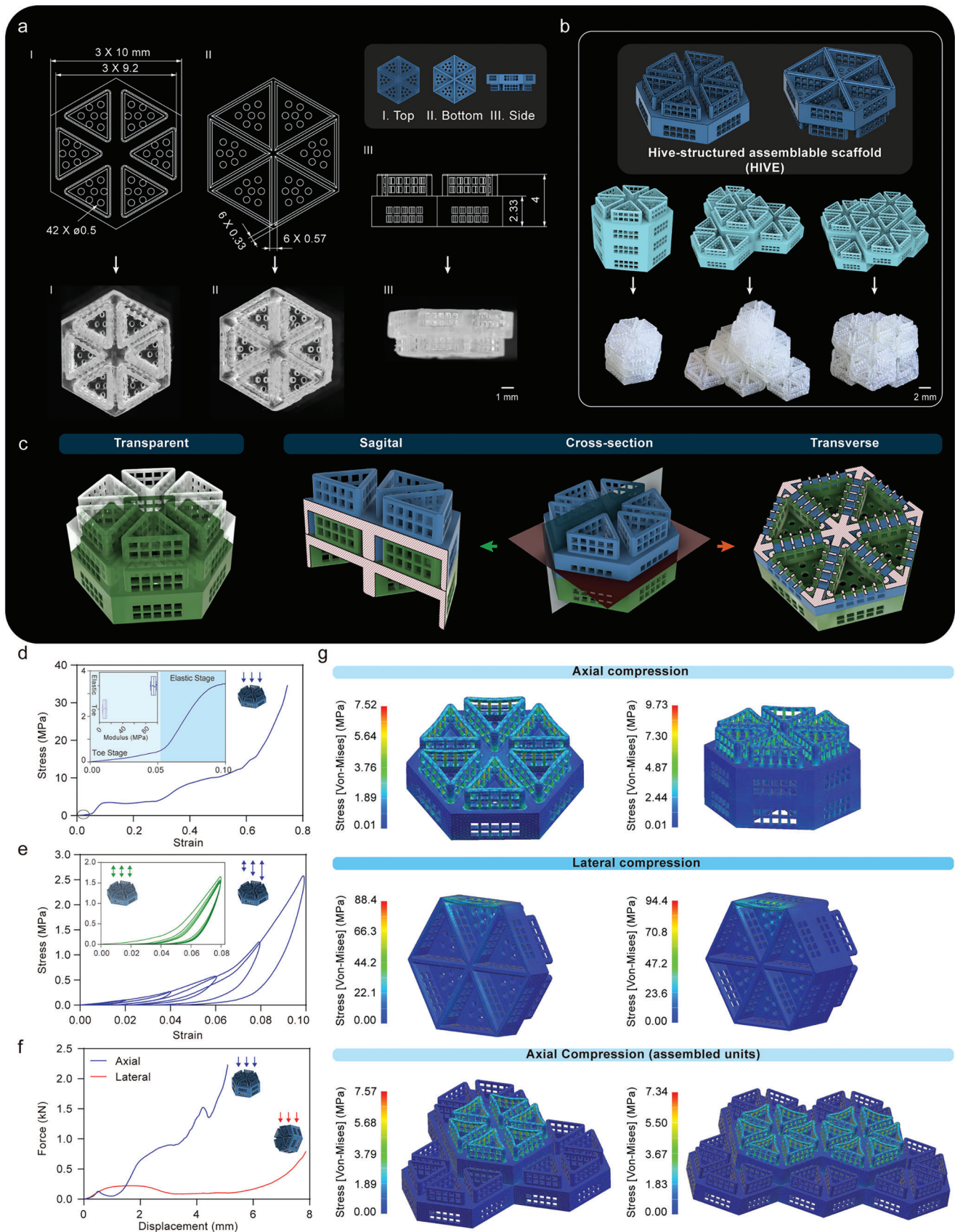
any defects at both the macro- and micro-level (Figure 2a; Figure S1, Supporting Information). For the assembly, the hollow triangular protrusion on the top of the HIVE interlocked precisely with the concave region at the bottom of the mating part by simply positioning one above the other and pressing manually. All HIVE scaffolds were precisely printed and allowed assembly in any shape or size with ease. As shown in Figure 2b, the scaffolds could be assembled in a multistacked form with various dimensions by simple click-assembly, for example forming a straight-lined implant for a long defect, a pyramidal shape, and a stacked implant for a complex-shaped defect. Additionally, we assembled HIVE scaffolds to demonstrate the possible implants that can be applied in several medical applications such as mandibular reconstruction and spinal fusion surgery (Figure S2a, Supporting Information). Furthermore, to assess the printability and material compatibility of the HIVE design, we conducted 3D printing experiments using different materials and printing methods. As shown in Figure S2b (Supporting Information), we successfully 3D-printed HIVE scaffolds in various scales using poly(lactic acid) with fused deposition modeling and different resins with DLP, confirming the printability and material compatibility of the HIVE design. Likewise, numerous configurations are possible with just a single HIVE design, showing the potential for affordable and off-the-shelf patient-specific treatments. In addition, the inner structure of HIVE was investigated after assembly, as the designed structure governs cellular activity and migration for bone formation. As shown in Figure 2c, the sagittal and the transverse cross-section of HIVE demonstrate highly interconnected porous structures which could promote cell migration, nutrition flow, and vascularization. We additionally investigated the stability of HIVE in a simulated physiological environment using PBS over a period of 70 days (Figure S3, Supporting Information). As we selected a biocompatible and biodegradable resin material, HIVE exhibited a gradual degradation process, albeit at a slow rate, with ≈97.6 ± 0.4% of the initial mass remaining after 70 days. This degradation rate was comparatively higher than that observed with conventional resin materials, which are known to be non-biodegradable. The ability of the HIVE scaffold to degrade in a controlled manner is advantageous, as it can provide consistent structural support during the process of osseointegration, while concurrently creating space for optimal bone formation over time.

2.2. Mechanical Durability and Finite Element Analysis of HIVE

In order to investigate the mechanical properties of HIVE as an implant, first, compression tests on a single HIVE were performed. As shown in the stress vs strain curve of HIVE, a toe region and an elastic region within 10% strain were observed (Figure 2d). From the curves, the moduli were calculated to be 9.75 ± 3.40 and 93.4 ± 4.23 MPa for the toe region (0–5% strain) and elastic region (5–10% strain), respectively. To confirm the mechanical stability of HIVE, the single scaffold was tested under cyclic compressive loading to a predefined strain of 8% or under progressive loading to a maximum strain of 10%. As shown in the stress vs strain curves in Figure 2e, the samples maintained their integrity under both cyclic loading and progressive loading. In addition, a hysteresis loop was observed, indicating an energy dissipation. The mechanical strength of the HIVEs in assembled configurations was also investigated under both axial and lateral compression. Based on the force vs displacement curve of HIVEs, the assembled HIVE scaffolds exhibited higher stiffness and strength in axial compression compared to lateral compression (Figure 2f). All HIVE were ductile and no brittle fracture was observed in the tests.

Next, finite element analysis (FEA) was performed to examine the mechanical stability of the HIVEs in both single and assembled unit configurations under simulated physiological loading, with spinal fusion as the exemplary indication. A distributed pressure of 1.25 MPa, the maximum intradiscal pressure,[10] was applied in the axial or lateral direction. The results in Figure 2g illustrate that the maximum von Mises stresses in the single top-loaded scaffold reached 7.5 MPa and the sideloaded reached 88.4 MPa which were both below the flexural strength of the material. Most stress concentrations were identified around the pores, but the maximum von Mises stress is shown to be modest and lower than the flexural strength of the material which indicates the risk of permanent deformation. In addition, the assembled HIVE in various configurations was examined to check the difference in mechanical stability in the case of assembly. The results of the assembled system with two HIVEs demonstrated a similar stress distribution compared to the single-loaded scaffold under both axial and lateral compression; the side-loaded scaffold showed higher stress concentrations compared to the top-loaded scaffold, and no stress concentrations at the interfaces between the stacked scaffolds were observed. Additionally, in the case of two complex assemblies which were symmetric and asymmetric assembly configurations, a maximum von Mises stress of ≈7.34–7.57 MPa was predicted, with stress concentrations accumulating around the pores. Then, we compared the mechanical stability of the HIVE, assemblable scaffold, and a conventional 3D-printed scaffold of the same overall shape. A triple-stacked configuration resembling a bulk conventional 3D-printed scaffold was simulated and compared with triple-stacked HIVE. As shown in Figure S4 (Supporting Information), the conventional scaffold showed slightly higher von Mises stresses compared to

Figure 2. Design and mechanical characterization of HIVE. a) Representative design and microscopy images of a single HIVE scaffold with dimensions, from different perspectives. b) Orthogonal projection of 3D designs of a single HIVE unit and 3D images/photographs of HIVE scaffolds assembled in various forms. c) 3D diagrams of two assembled HIVE scaffolds with the sagittal (gray plane, left) and the transverse (red plane, right) cross-section of assembled scaffolds demonstrating the interconnected porous structure. d–f) Mechanical properties of HIVE scaffolds. Images of HIVE with arrows represent the load case. d) Representative stress–strain curve of HIVE scaffolds under vertical compression. The inner box magnifies the circled region of the curve (strain of 0–0.1) with the graph of elastic modulus at the toe and elastic region. e) Representative stress–strain curve of a single HIVE scaffold under cyclic (green) and progressive compressive loading (blue). f) Representative force–displacement curve of two assembled HIVE scaffolds under axial (blue) and lateral (red) compression. The arrows represent the direction of the loading. g) FEA of single and assembled HIVE scaffolds under 1.25 MPa, maximum intradiscal pressure, as an exemplary indication for spinal fusion application. The pressure load was applied on the top surface of the scaffold with the bottom surface fully constrained.

**ADVANCED
SCIENCE NEWS**

www.advancedsciencenews.com

**ADVANCED
MATERIALS**

www.advmat.de

HIVE in both top and side loading scenarios, but the stress distributions of the conventional scaffold are similar compared to the assemblable scaffold. Based on mechanical testing and FEA, HIVE in various configurations has demonstrated adequate mechanical durability to withstand loading in the physiological system and also shows comparable mechanical stability as the conventional bulk scaffold.

2.3. Osteogenic Capacity of HIVE System as a Growth Factor Carrier (BMP-2)

After the development of HIVE, we augmented the scaffold with one more component, a gelatin/heparin MC which has been developed in our previous study.[1d,8] The macroporous and interconnected structure of MC was fabricated by lyophilizing ice crystals formed during the ethyl(dimethylamino propyl)carbodiimide/N-hydroxysuccinimide (EDC/NHS) crosslinking between gelatin and heparin at $-20\ °C$ which enabled MC to have a biocompatible environment with enhanced cell migration. As shown in **Figure 3**a, due to the sponge-like structure and its shape-recovery functionality,[8] MCs were easily loaded in the pockets of HIVE without any deformation or loss of material. Then, these prepared MCs can be reinforced with several biological factors such as GFs, bioceramics, or cells and embedded in each pocket of 3D-printed HIVE (Figure 1). This complete HIVE system (HIVE/MC) can work as a carrier for a specific treatment as the user targets his or her choice of biothislogical factors.

As a first step, we investigated the capacity of HIVE/MC as a GF carrier system using BMP-2 or VEGF (Figure 3b). Thus, the drug release kinetics of the HIVE/MC was examined first by using fluorescein isothiocyanate-labeled bovine serum albumin (FITC-BSA). Briefly, 0.01% (w/v) FITC-BSA was loaded to six dehydrated MCs, and the MCs were put in the pocket of HIVE (H+MC6). For the blank HIVE group (a HIVE group without MCs), the same amount of proteins were loaded on the center of each pocket of HIVE to initiate physical adsorption. Then, we compared the release rate of protein between blank HIVE and H+MC6. The release of FITC-BSA was measured by fluorescence spectroscopy and as shown in Figure S5 (Supporting Information), for the blank HIVE group, ≈65% of FITC-BSA was cumulatively released by 5 days and ≈80% was released by 13 days. Meanwhile, H+MC6 released ≈50% by 5 days and 60% by 13 days which indicates that the structural design of the HIVE/MC enabled a slower release profile than the blank HIVE group. Then, in order to verify the sustained release GF kinetics of the HIVE/MC due to heparin-binding affinity from MC, we tested with BMP-2, an osteogenic GF, and VEGF, an angiogenic GF. 100 ng mL^{-1} of BMP-2 or VEGF was loaded to HIVE and H+MC6 in a similar method to the prior experiment, and released GFs were measured using enzyme-linked immunoassay (ELISA). For BMP-2, HIVE showed the burst release profile by releasing 63% and 78% within 5 and 13 days respectively (Figure 3c). On the other hand, H+MC6 demonstrated a steady and significantly slower release rate compared to the HIVE group by releasing 19% and 28% within 5 and 13 days. Even until day 35, H+MC6 accumulatively released only 38% of BMP-2 while the HIVE group released 85%. In the case of VEGF, a similar

release profile was measured that HIVE and H+MC6 released ≈76% and 25% respectively within 13 days (Figure 3d). These experiments with BMP-2 and VEGF demonstrated a successfully controlled drug release profile of the HIVE/MC mainly due to the heparin-binding affinity to BMP-2 and VEGF. So this system would enable steady release of BMP-2 and VEGF to enhance tissue formation by inducing osteogenesis and angiogenesis in an efficient way, which led us to confirm their in vitro capacity.

In order to compare the osteogenic effect from HIVE/MC with different numbers of MCs, we defined four groups: HIVE as a blank HIVE, H+MC1, MC3, and MC6 as a HIVE/MC with a biological factor loaded—1 MC, 3 MC, and 6 MCs respectively. First, we treated hMSC with osteogenic medium (OM) in the presence of BMP-2-loaded HIVE groups and checked alkaline phosphatase (ALP) activity by ALP staining on day 7 and calcium deposition by Alizarin Red S (ARS) staining on day 14. As shown in Figure 3e,f, HIVE groups with more MCs in the initial stage showed a higher level of osteogenesis with higher ALP activity. Similarly, ARS staining results also showed that the group with more MCs showed a higher level of calcification (**Figure 4**g,h; Figure S6, Supporting Information). In particular, the H+MC6 group showed significantly higher levels of osteogenesis and calcification among the group. In the case of H+MC1, despite its low number of MC, the group demonstrated a significantly higher level of osteogenesis than the blank HIVE which indicates that one MC can already induce the osteogenic effect of the scaffold. The ALP and ARS histological results were further confirmed by quantitative real-time polymerase chain reaction (RT-qPCR) analysis of osteogenic gene markers. In line with ALP and ARS results, the HIVE groups with more MCs showed a higher expression of osteogenic gene markers *ALP*, *COL1*, *RUNX2*, and *OCN* on both day 7 and day 14 (Figure 3i). On day 7, H+MC3 and H+MC6 showed a similar degree of osteogenic gene upregulation, however, on day 14, H+MC6 showed the highest expression of ALP, COL1, RUNX2, and OCN with 8.1 ± 0.3, 2.8 ± 0.1, 5.5 ± 0.8 and 7.9 ± 0.5-fold higher compared to those of HIVE group respectively. Likewise, H+MC3 showed the second-highest osteogenic gene upregulation among the groups. From the comprehensive results from ALP, ARS, and RT-qPCR, we observed that the sustained release of BMP-2 and the biocompatible and porous structure of MCs enhanced the osteogenic capacity of HIVE/MC and confirmed its potential as a BMP-2 carrier as well.

2.4. Angiogenic Capacity of HIVE System as a GF Carrier (VEGF)

Next, we validated the angiogenic capacity of HIVE/MC as a VEGF carrier in a similar method as experiments for the BMP-2 carrier. For this study, HUVEC were cultured in the conditioned medium which was prepared by incubating HIVE groups with VEGF-loaded MCs in HUVEC growth medium. Then, with these primed cells, the tube formation assay and the wound-healing migration assay were conducted to confirm the angiogenic effect of VEGF continuously released from HIVE/MC groups. First, for tube formation assay, primed HUVECs were seeded on the Matrigel matrix and the tube formation was observed for 10 hours. As shown in Figure 3j and Figure S7 (Supporting Information), the HIVE group with more MCs demonstrated superior

**ADVANCED
SCIENCE NEWS**

www.advancedsciencenews.com

**ADVANCED
MATERIALS**

www.advmat.de
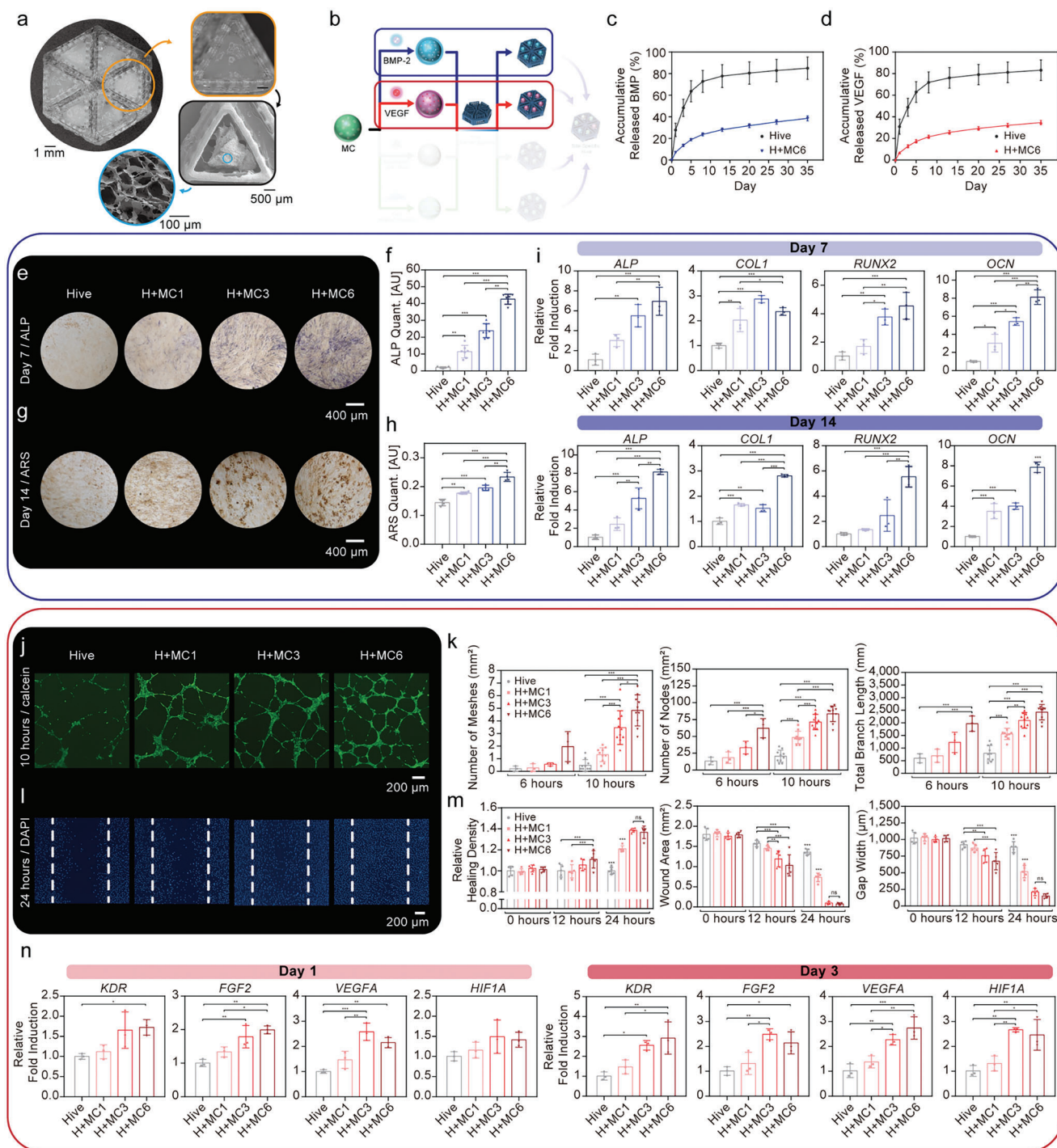
Figure 3. HIVE system as a selective growth factor (GF) carrier. a) Representative images of HIVE system (HIVE/MC). The right two images show the light microscopy and SEM images of a single pocket loaded with MC (scale bar: 500 μm). The SEM image shows the lyophilized HIVE/MC and the bottom-left blue-highlighted circle image shows the cross-section of lyophilized MC to demonstrate the macroporous structure. b) Schematic illustration of HIVE with BMP-2- or VEGF-loaded MC system c,d) Release profile of BMP-2 (c) or VEGF (d) on HIVE and H+MC6 for 35 days. 200 ng mL^{-1} of BMP-2 or VEGF was loaded in scaffolds in the same way as the FITC-BSA experiment. e–i) Osteogenic differentiation of HIVE system as a BMP-2 carrier. hMSCs were cultured with the OM and BMP-2 released from HIVE for 7 days. e–h) Representative images and quantitative analysis of ALP (e,f) and ARS (g,h) staining after 7 or 14 days of osteogenic differentiation. i) Relative fold induction of osteogenic genes on days 7 and 14. j–n) The angiogenic capacity of the HIVE system as a VEGF carrier. HUVECs were cultured with the HUVEC medium and VEGF was released from HIVE for 7 days. j) Representative images of tube formation assay and k) quantitative analysis that shows the number of meshes, nodes, and total branch length from tube formation. l) Representative images of wound-healing migration assay and m) quantitative analysis that shows relative healing density, wound area, and gap width. n) Relative fold induction of angiogenic genes on days 1 and 3. In the testing groups, MC1, MC3, and MC6 represent the number of MCs filled in the pocket of HIVE. The error bars indicate SD; $n = 3$.
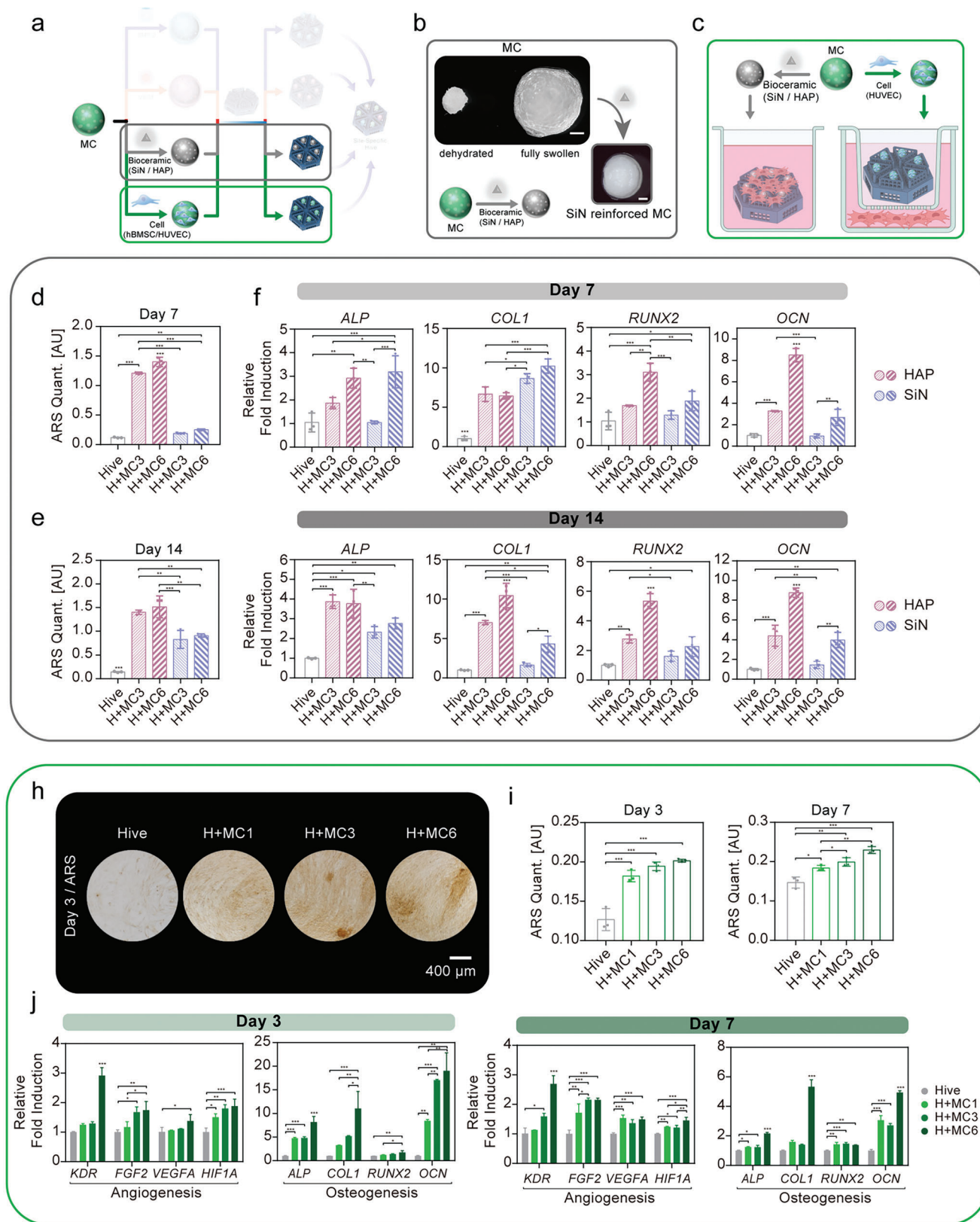
Figure 4. HIVE system as a selective bioceramic and cell carrier a) Schematic illustration of HIVE with bioceramic or cell-loaded MC system b) Representative microscopy images of MC and SiN reinforced cryogel. Scale bar: 500 µm c) Illustration of in vitro experiments using HIVE with different MC systems. For HIVE as a bioceramic carrier, hMSCs were cultured on the scaffolds with the OM, and for HIVE as a HUVEC carrier, hMSCs were co-

**ADVANCED
SCIENCE NEWS**

www.advancedsciencenews.com

**ADVANCED
MATERIALS**

www.advmat.de

tube formation in 10 hours. At 6 h, there was already some tube formation difference between the HIVE group and H+MC groups except H+MC1, and the greater difference was observed at 10 hours even between H+MC1 and HIVE groups. Quantified data based on images such as the number of meshes, nodes, and branch length also confirmed successful tube formation in H+MC groups, particularly H+MC3 and H+MC6 (Figure 3k). For the wound-healing assay, a straight scratch was made on the cell culture plate that is confluent with HUVECs and then, the cell migration was observed for 24 h. As shown in Figure 3l and Figure S8 (Supporting Information), HUVECs incubated in HIVE/MC groups with more VEGF-loaded MC demonstrated higher cell migrations and wound healing rates than those in the blank HIVE group. Especially, at 24 h, both H+MC3 and H+MC6 showed a significantly higher healing rate, resulting in closed wounds. Light microscopy images and DAPI-stained cell images were used to quantify the response, such as relative healing density, wound area, and gap width, and the results also confirmed a rapid recovery of scratched distance in the HIVE/MC groups (Figure 3m). Also, there was no significant difference between H+MC3 and H+MC6 at 24 h. Finally, the results were also validated by RT-qPCR analysis of angiogenic gene markers. H+MC3 and H+MC6 groups represented a higher expression of angiogenic gene markers *KDR, FGF2, VEGFA,* and *HIF1A* at similar degrees on both days 1 and 3 (Figure 3n). Especially, on day 3, H+MC6 showed the most upregulated angiogenesis marker *KDR, FGF2, VEGFA,* and *HIF1A,* with 2.9 ± 0.8-, 2.1 ± 0.5-, 2.2 ± 0.2-, and 2.5 ± 0.6-fold higher compared to those of HIVE group respectively. In line with the wound-healing assay result, H+MC3 showed the second-highest angiogenic gene upregulation with no significant difference with H+MC6 which indicates the 3 MCs would be enough to bring therapeutic effect in the aspect of angiogenesis and wound-healing. Overall, based on the experimental results with HIVE/MC and HUVEC, we observed the potential of HIVE/MC as a VEGF carrier by providing sustained continuously released VEGF which would bring positive response of HUVEC and induce the neovascularization for enhanced tissue regeneration.

2.5. Osteogenic Effect of HIVE System as a Bioceramic Carrier (HAP & SiN)

As a next step, the potential of the HIVE system as a bioceramic carrier was investigated (Figure 4a). In this HIVE/MC, we used hydroxyapatite (HAP) or silicon nitride (SiN) reinforced MC which has been developed in our previous studies.[11] We chose a 20% (w/v) concentration of bioceramic for reinforcement, which has shown the highest osteogenic effect and efficiency. As shown in Figure 4b, MC demonstrates a spherical shape with a transparent color, while the color of the MC gets whiter as the SiN microparticles are loaded, which indicates the successful incorporation of SiN into MC. However, despite the reinforcement of bioceramics, characteristics and morphology of HAP or SiN-loaded

MC such as their sponge-like properties were not affected and still provided a hydrophilic, biocompatible, and macroporous environment to cells. First, we defined five testing groups: HIVE as a blank HIVE, H+MC3 (HAP- or SiN-loaded), and H+MC6 (HAP- or SiN-loaded) and seeded the hMSCs on samples to investigate the osteogenic effects of HIVE/MC as a bioceramic carrier (Figure 4c). ARS stainings and RT-qPCR were carried out to check calcium deposition and osteogenic gene expression after culturing hMSC-laden scaffolds with OM for 7 and 14 days. For ARS, both H+MC3 and H+MC6 with HAP and SiN-reinforced MCs demonstrated significantly higher calcium deposition on day 7 and day 14 compared to blank HIVE (Figure 4d,e). Especially, HIVE/MC groups with HAP-reinforced MCs showed the highest mineralizations among the group. In addition, there was no significant difference between H+MC3 and H+MC6 regardless of which bioceramic we used. This suggests that 3 bioceramic reinforced MCs in HIVE can achieve a similar level of mineralization as the H+MC6 group. Then, we further focused on the osteogenesis of hMSCs by RT-qPCR. In line with ARS analysis, both HAP or SiN-loaded HIVE/MC groups upregulated osteogenic gene expressions compared to the control group (Figure 4f). Interestingly, on day 7, the SiN-loaded H+MC6 group demonstrated the highest expression of osteogenic marker *ALP* and *COL1* while the HAP-loaded H+MC6 group demonstrated the highest expression of marker *RUNX2* and *OCN*. However, on day 14, HAP-loaded H+MC6 exhibited the highest expression of osteogenic gene markers *ALP, COL1, RUNX2* and *OCN,* with 3.8 ± 0.7-, 10.4 ± 1.6-, 5.3 ± 0.5-, and 8.8 ± 0.5-fold higher compared to those of control group respectively. Meanwhile, SiN-loaded H+MC6 showed an upregulation of osteogenic genes, but lower than that of HAP-loaded H+MC3. We noted an enhanced osteogenic effect from HIVE/MC with both HAP and SiN-reinforced MC due to the biocompatible environment from MC and osteoconductivity from both bioceramics. Overall, this suggests another potential of HIVE/MC, that it can also be utilized as a bioceramic carrier.

2.6. Angiogenic-Osteogenic Potential of HIVE System as a Cell Carrier (HUVEC)

Next, the HIVE/MC was examined to see its potential for cell delivery functionality. We seeded HUVECs on MCs and put these cell-laden MCs in an HIVE to test as a HUVEC carrier (Figure 4a). In order to evaluate the cellular effect from HIVE/MC as a HUVEC carrier, we co-cultured hMSCs on a cell culture plate and HIVE/MC with HUVEC-laden MCs using a transwell as shown in Figure 4c. Then, we checked the cellular response of hMSCs, and whether this HUVEC carrier can induce angiogenic and osteogenic effects in the cells. First, the calcium deposition of hMSCs was checked by ARS staining after co-culturing for 3 and 7 days. As shown in the microscopy image and quantitative data, all HIVE with MC groups showed enhanced mineralization compared to the control group on both days 3 and 7

cultured on the plate in the presence of HUVEC laden HIVE system in transwell. d–f) Osteogenic differentiation of HIVE system as a HAP or SiN carrier. d,e) Quantitative analysis of ARS staining after 7 or 14 days. f) Relative fold induction of osteogenic genes on days 7 and 14. h–j) Osteogenic effect of HIVE system when used as a HUVEC carrier. h) Representative images and i) quantitative analysis of ARS staining. j) Relative fold induction of angiogenic and osteogenic genes of hMSCs on days 3 and 7. The error bars indicate SD; $n = 3$.

**ADVANCED
SCIENCE NEWS**

www.advancedsciencenews.com

**ADVANCED
MATERIALS**

www.advmat.de

(Figure 4h,i; Figure S6, Supporting Information). Interestingly, the H+MC1 group showed significantly higher calcium deposition than the control group from day 3, which indicates that even one HUVEC-laden MC was effective in inducing mineralization. Then, RT-qPCR was used to investigate the angiogenic and osteogenic gene expression of hMSCs. On day 3, H+MC6 was the group with the highest expression of angiogenic gene markers *KDR, FGF2, VEGFA* and *HIF1A*, with 2.9 ± 0.3-, 1.7 ± 0.3-, 1.4 ± 0.2-, and 1.9 ± 0.2-fold higher and osteogenic gene markers *ALP, COL1, RUNX2* and *OCN*, with 8.2 ± 1.2-, 11.1 ± 3.6-, 1.8 ± 0.4-, and 19.0 ± 3.8-fold higher compared to the control group (Figure 4j). Furthermore, H+MC3 demonstrated a certain level of angiogenesis and osteogenesis while H+MC1 showed a relatively low effect and upregulations in only *HIF1A* and *ALP*. On day 7, all H+MC groups verified upregulation in angiogenic and osteogenic gene expressions, and H+MC6 still represented the group with the highest angio–osteogenic gene expressions. However, unlike day 3, the H+MC1 and H+MC3 groups exhibited a similar degree of angio–osteogenic gene expression as that of H+MC6. Especially, there was no significant difference among H+MC groups in some gene markers such as *VEGFA* and *RUNX2*. These results on day 7 could be likely due to the increased number of HUVECs from 7 days of proliferation on MCs in H+MC1 and MC3. Overall, based on the ARS and PCR results, we verified the possible use of HIVE/MC as a cell carrier that can bring both angiogenic and osteogenic effects on the targeted tissues for regeneration.

2.7. Multifunctional and Site-Specific Effect of HIVE System

After examining various potentials of HIVE/MC as carrier systems, we investigated the multifunctional effect and cellular response when MCs loaded with various biological factors are combined in a single HIVE. So we developed a Mix-HIVE/MC group, a new HIVE/MC group with 2 BMP-loaded MCs, 2 VEGF-loaded MCs, and 2 SiN-loaded MCs as shown in **Figure 5**a. In order to check the synergistic effect of combining different MCs, we compared it with blank HIVE and other HIVE/MC filled with only BMP-, VEGF-, and SiN-loaded 6 MCs: BMP-HIVE/MC, VEGF-HIVE/MC, and SiN-HIVE/MC respectively. In this study, we used SiN for the bioceramic group due to its excellent potential as a bioceramic for orthopedic implants, such as a similar degree of osteoconductivity as HAP, but with an additional antibacterial effect that was shown in other research.[11a,12] Then, we seeded hMSCs on the testing groups and checked calcium deposition and osteogenic gene expression after culturing them in OM for 7 and 14 days. On day 7, all HIVE/MC groups showed significantly higher calcium deposition compared to the control group, and especially, Mix-HIVE/MC showed the highest mineralization (Figure S9, Supporting Information). Similarly, RT-qPCR analysis on day 7 also showed the corresponding result that Mix-HIVE/MC significantly upregulated most osteogenic gene markers *ALP, RUNX2*, and *OCN* (Figure S10, Supporting Information). On the other hand, other HIVE/MC groups such as BMP-HIVE/MC, VEGF-HIVE/MC, and SiN-HIVE/MC showed insignificant differences in upregulations of *COL1, RUNX2*, and *OCN*. Unlike results on day 7, as shown in Figure 5b,c, all HIVE/MC groups showed significantly higher calcium deposi-

tion and osteogenic gene expressions compared to the control group on day 14. BMP-HIVE/MC exhibited the second-highest osteogenesis and mineralization among the groups, and especially, Mix-HIVE/MC exhibited the highest expression of osteogenic gene markers *ALP, COL1, RUNX2*, and *OCN*, with 20.2 ± 3.7-, 26.0 ± 2.1-, 7.6 ± 1.0-, and 8.0 ± 0.7-fold higher compared to those of the control group, respectively. These results suggest that enhanced osteogenesis in Mix-HIVE/MC can be achieved due to synergistic effects from combining BMP-, VEGF-, and SiN-loaded MCs in a single HIVE and this system can be worked as another solution for bone regeneration.

After confirming the synergistic effect from Mix-HIVE/MC, the next question we had was whether there would be a site-specific effect at the locations where different MCs were located. Therefore, the site-specific effects of Mix-HIVE/MC at the micro-level were scrutinized. After culturing hMSC-laden Mix-HIVE/MC with OM for 2 weeks, we used a surgical blade to isolate the scaffold into three sites: BMP-, VEGF-, and SiN-sites where each specific MCs were located, respectively (Figure 5d). Then, we analyzed the osteogenic gene expressions of hMSCs from each site by using RT-qPCR. Some differences in osteogenesis were observed between the sites. As Figure 5e shows, the BMP-site and SiN-site of Mix-HIVE/MC showed upregulated osteogenic gene expressions of a similar degree. Interestingly, the SiN-site exhibited the highest expression of osteogenic gene markers *RUNX2* and *OCN*, with 6.0 ± 0.4- and 4.3 ± 0.5-fold higher while the BMP-site exhibited the highest expression in markers *ALP* and *COL1*, with 3.7 ± 0.1- and 4.8 ± 0.5-fold higher compared to those of control group respectively. The overall results demonstrated distinct differences in osteogenic gene expression from different sites which suggest the potential of the HIVE system to allow site-specific treatment even at the micro-level.

2.8. Cell Morphology and Migration on Assembled HIVE

After checking the potential of the HIVE as a multifunctional carrier system, we studied the cellular response, such as morphology and migration on the HIVE/MC. First, for the cell morphology, cells seeded on single HIVE/MC were observed via actin and Dapi staining after 7 days of culturing. Various confocal laser scanning microscopy (CLSM) images of cells at different regions of HIVE/MC were examined, and despite its complex structure, as shown in Figure 5f, cells on HIVE/MC were well attached and exhibited round, polygonal morphology with distinct and thick stress fibers. Cells were homogenously spread on all regions of the HIVE exoskeleton including top and side walls (Figure 5f-I,VIII), the corner region at the pocket (IV), and pore regions (III, VI). Furthermore, cells were not only well attached and proliferating on the MCs (II), but also bridging between the MC and HIVE (V) and between pockets of the HIVE (VII).

Cell migration between HIVEs in the case of assemblies was evaluated. First, hMSCs were seeded on a single HIVE and after cell attachment, the cell-laden HIVE was stacked on top of an acellular HIVE in order to assemble them (Figure 5g). Then, cell migration between the HIVEs was observed after 7 days of culturing in GM. As shown in the CLSM image, although the number of cells on the bottom HIVE is fewer than on the top HIVE,
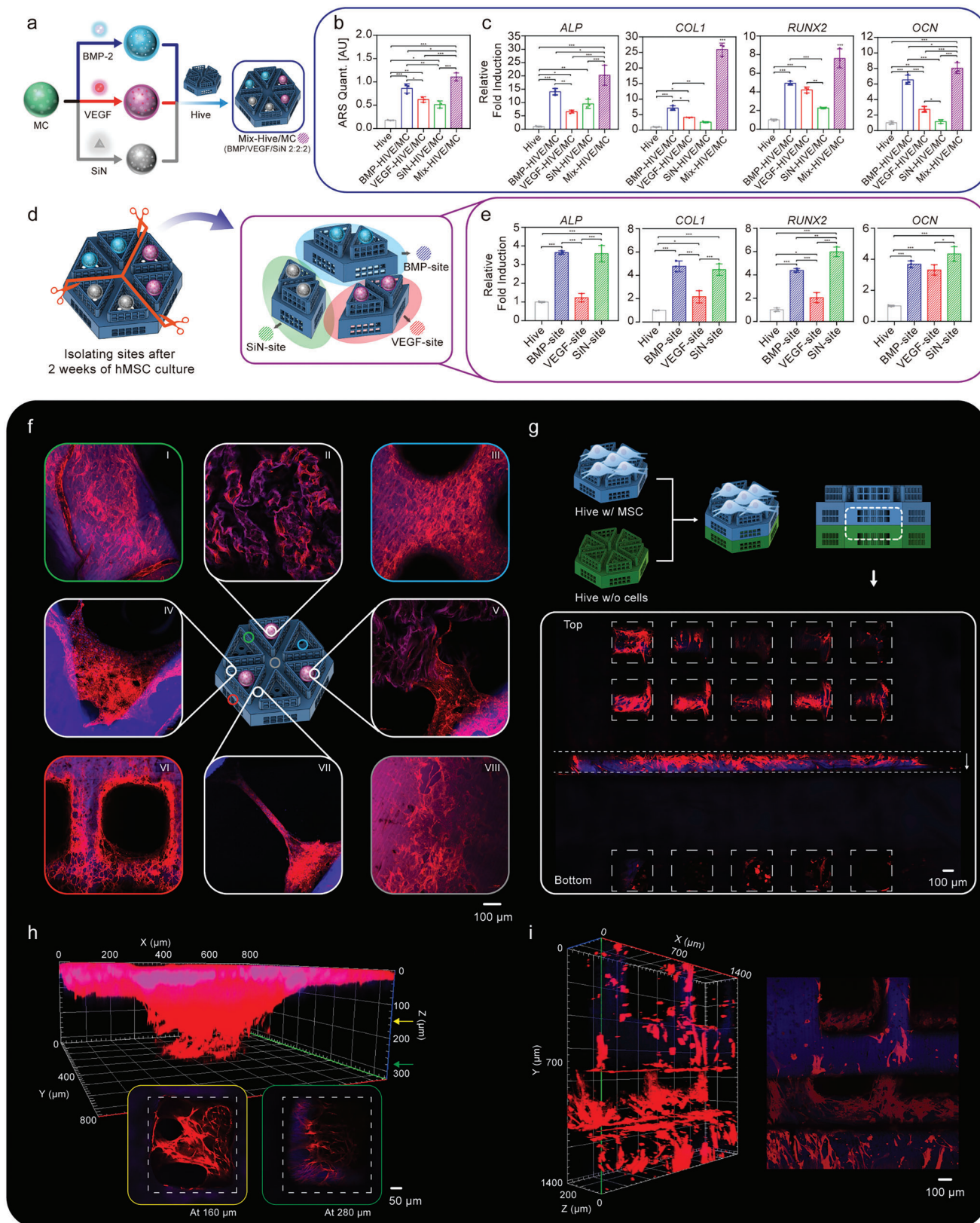
Figure 5. Site-specific and multifunctionality of HIVE and cellular activity in case of assembly. a) Schematic illustration of multifunctional HIVE with MCs loaded with BMP-2, VEGF, or SiN. b,c) Comparison of osteogenesis in HIVE systems with different MCs. All testing groups had six MCs in each HIVE, and the Mix-HIVE/MC group had two BMP-2, two VEGF, and two SiN-loaded MCs. hMSCs were cultured on the scaffolds with the OM for 14 days.

**ADVANCED
SCIENCE NEWS**

www.advancedsciencenews.com

**ADVANCED
MATERIALS**

www.advmat.de

homogenously spread cells were observed at all the pores of the bottom HIVE. This indicates that cell migration between HIVEs in assembled configurations was successful. Also, 3D Z-stacked images of cells at the pore region of the HIVE demonstrated that cells are proliferating and migrating from the outer surface to the inner structure via the pores (Figure 5h). It was also verified by the cross-section images of cells at different pore depths, which were 160 and 280 µm. Furthermore, as shown in Figure 5i, a 3D reconstructed image at the boundary region between assembled HIVEs represents successful cell migration on the surfaces of assembled HIVEs as well. These two images emphasize that cell migration can occur not only via the interconnected pores but also over the surfaces between the assembled HIVEs. Overall, it suggests that successful cell attachment and migration between HIVEs will provide enhanced tissue formation and eventually osseointegration even in the case of complex assemblies.

2.9. In Vivo Subcutaneous Implantation in Rats

To demonstrate the functionality of the HIVE, a subcutaneous implantation was performed. As described in **Figure 6**a, HIVE/MC groups (HIVE/MC, BMP-HIVE/MC, VEGF-HIVE/MC, SiN-HIVE/MC and Mix-HIVE/MC (2 BMP: 2 VEGF: 2SiN)) were placed in subcutaneous pockets of 8-week-old rats, and the samples were collected 4 weeks after surgery to compare the biocompatibility, cell migration, angiogenesis and possible bone formation. Rats did not show any symptom of inflammation and especially, the photographs of harvested samples showed that all groups showed nice tissue formation within the scaffolds and no sign of severe inflammation (Figure 6b). Especially, in the group with GFs such as VEGF, we confirmed tissues with redness on the scaffold which indicates successful vascularization. In order to scrutinize the biological response in a microscopic level, hematoxylin and eosin (H&E) and Masson's trichrome (MTC) staining was performed for histological analysis.

Based on the H&E staining analysis, we confirmed high biocompatibility, cell migrations, and ECM formations from all HIVE groups including HIVE/MC as a control (Figure 6c). Among the groups, BMP-HIVE/MC and Mix-HIVE/MC groups showed the most distinguished cell migrations and dense collagen tissue formation, and especially, the BMP site and SiN site from Mix-HIVE/MC group showed thick tissue formation compared to the VEGF site. On the other hand, in terms of angiogenesis, VEGF-HIVE/MC and Mix-HIVE/MC groups demonstrated a high level of vascularization within the scaffold by showing the presence of red blood cells and structures clearly resembling blood vessels. In MTC staining analysis, we found similar results as those from H&E staining by confirming thick collagen tissue formation in BMP-HIVE/MC and Mix-HIVE/MC groups and blood vessel structures with red blood cells in VEGF-HIVE/MC and Mix-HIVE/MC groups (Figure 6d). From both H&E and MTC staining, VEGF-HIVE/MC and SiN-HIVE/MC exhibited distinctly higher levels of collagen formation than that of HIVE/MC, but lower compared to that of BMP-HIVE/MC or Mix-HIVE/MC. Additionally, both histological analyses demonstrated that the Mix-HIVE/MC group showed the densest collagen tissue formation and cell migrations into scaffolds compared to the rest of the groups. In addition, we analyzed the cross-sections of various regions in GF-loaded HIVE/MC systems to check tissue formation and cell migration at pore sites and interfaces between MC and 3D-printed struts (Figure 6e). As shown in Figure 6e-I, collagen tissue formation and cell migration were observed in the region between pockets of HIVE/MC. Additionally, dense tissue formation including even microvessels filled the voids between struts and MCs (Figure 6e-II,III). Smooth and stable tissue connections at the interface between MCs and voids or struts were found which indicates successful cell migrations within the scaffold. Similarly, vertical cross-sections of the scaffold also demonstrated cell migration within the pores by filling the pores with collagen and bridging between MC and the HIVE (Figure 6e-IV,V). This indicates the high biocompatibility of the HIVE/MC and the biological potential as GF carriers which would be effective enough to induce tissue formation at various parts of HIVE.

Then, to confirm the osteogenic and angiogenic capacity of HIVE at the microscopic level, ARS, toluidine blue, and cluster of differentiation 31 (CD31) stainings were performed for histological analysis (**Figure 7**). For bone formation, as shown in ARS-stained images and the quantified result of the mineralized area, HIVE/MC and VEGF-HIVE/MC showed almost no sign of mineralization while both BMP-HIVE/MC and Mix-HIVE/MC demonstrated the most mineralization within the scaffolds (Figure 7a,b). Also, SiN-HIVE/MC showed some mineralized areas which indicates successful osteogenesis from its osteoconductivity. Then, toluidine blue staining has been performed to compare the level of proteoglycans and glycosaminoglycans (GAGs). As shown in Figure 7c,d, HIVE/MC demonstrated the least toluidine-blue-positive area among the groups while BMP-HIVE/MC and Mix-HIVE/MC exhibited abundant presence of toluidine-blue-positive area within the scaffolds. Interestingly, unlike the ARS results, VEGF-HIVE/MC group presented significantly higher toluidine-blue-positive area which indicates that all groups except the HIVE group were able to induce the formation of proteoglycan and GAGs which are abundant in cartilage and bone tissues.

Last, CD31 staining was carried out to check the angiogenic potential of HIVE/MC. As shown in Figure 7e, HIVE/MC showed

b) Quantitative analysis of ARS staining and c) Relative fold induction of osteogenic genes on day 14. d) Illustration showing the investigation of the site-specific effect of the Mix-HIVE/MC group. hMSCs were seeded evenly on scaffolds and cultured for 2 weeks, and the scaffold was cut into three parts: BMP-, VEGF-, and SiN-site for analysis. e) Relative fold induction of osteogenic genes on isolated sites from the Mix-HIVE/MC group. f) Representative CLSM images that show the staining of actin microfilament cytoskeletal protein (red) and nuclei counterstained with DAPI (blue) of the cells after 7 days of culturing on the HIVE/MC system. g–i) g) CLSM image of cell migration from top scaffold to bottom scaffold after assembly and culturing for 7 days. First, hMSCs were seeded onto a single HIVE and cultured for 3 days. Then, the scaffold was assembled with HIVE which does not have cells attached, and stained with Phalloidin/DAPI after 7 days of culturing in assembled form. In the image, the white dashed lines represent the pores of the scaffold and the boundary of the top and bottom HIVEs. h) Z-stacked image that shows cell migration from outside to inside of the pore. i) 3D reconstructed image at the boundary region between top and bottom HIVEs.

**ADVANCED
SCIENCE NEWS**

www.advancedsciencenews.com

**ADVANCED
MATERIALS**

www.advmat.de
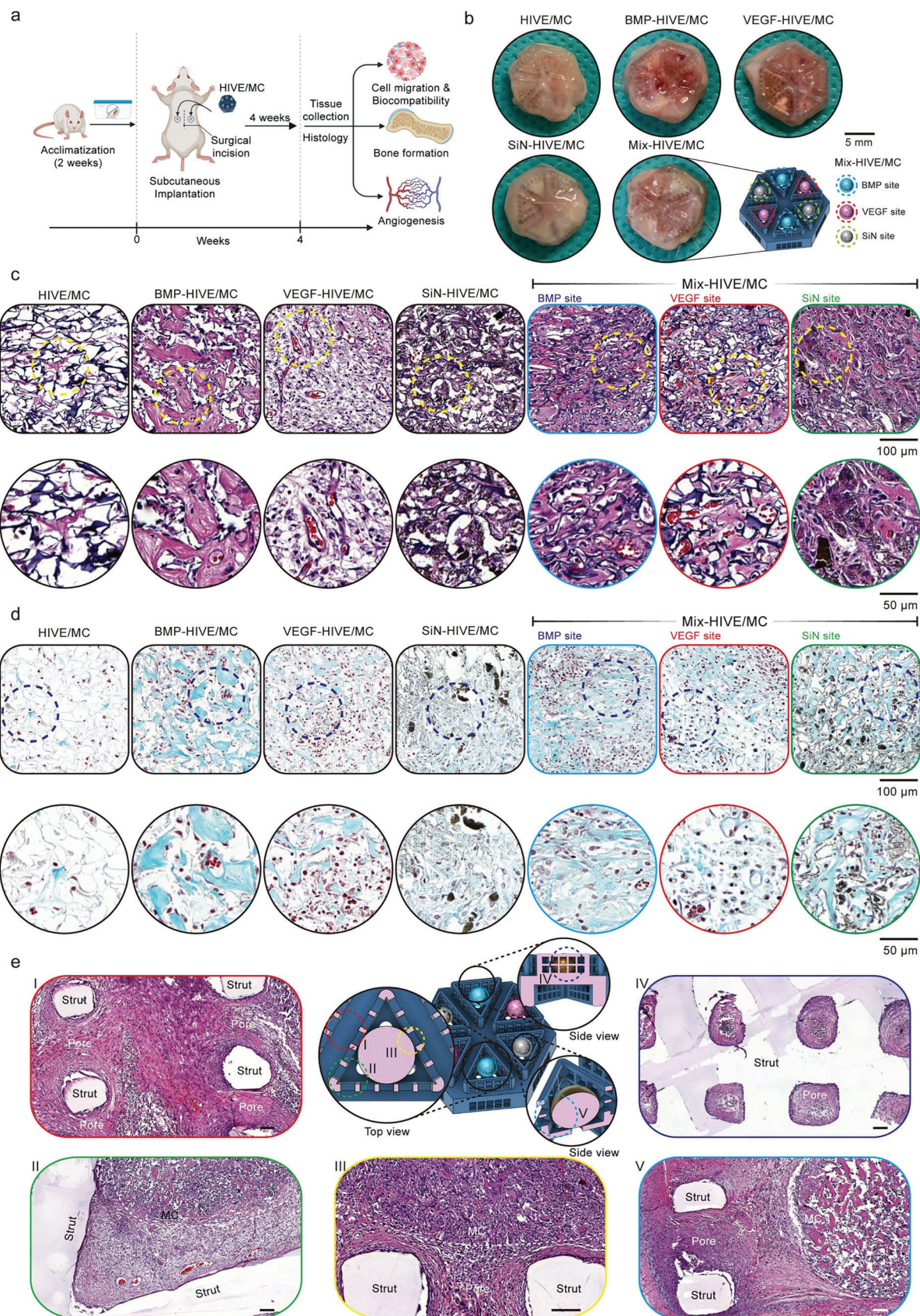
the least CD31-stained area, while VEGF-HIVE/MC and Mix-HIVE/MC groups exhibited abundant presence of CD31-positive blood vessel structures within the scaffolds. The BMP-HIVE/MC group also showed some CD31-stained areas and numbers of microvessel structures which indicates successful neovascularization. On the other hand, the SiN-HIVE/MC group exhibited the second-least CD31-stained areas with minor vessel structures among the groups. In quantified results, the average vessel perimeter and area also verified the histological analysis that all sites in Mix-HIVE/MC showed significantly higher vascularization compared to other groups (Figure 7f). In Mix-HIVE/MC, despite the difference is marginal, the VEGF site showed a higher vessel perimeter than the BMP or SiN site which confirms the site-specific effect in HIVE. Additionally, we confirmed that all GF- or bioceramic-loaded HIVE/MC groups exhibited significantly higher CD31-positive area than HIVE/MC, a negative control group (Figure 7g). Interestingly, in terms of CD31-positive area, the difference between VEGF-HIVE/MC and Mix-HIVE/MC was not statistically significant which suggests VEGF-HIVE/MC's angiogenic effect affected a broader area in the scaffold despite fewer microvessels while Mix-HIVE/MC's angiogenic effect focused on smaller area to yield more microvessels.
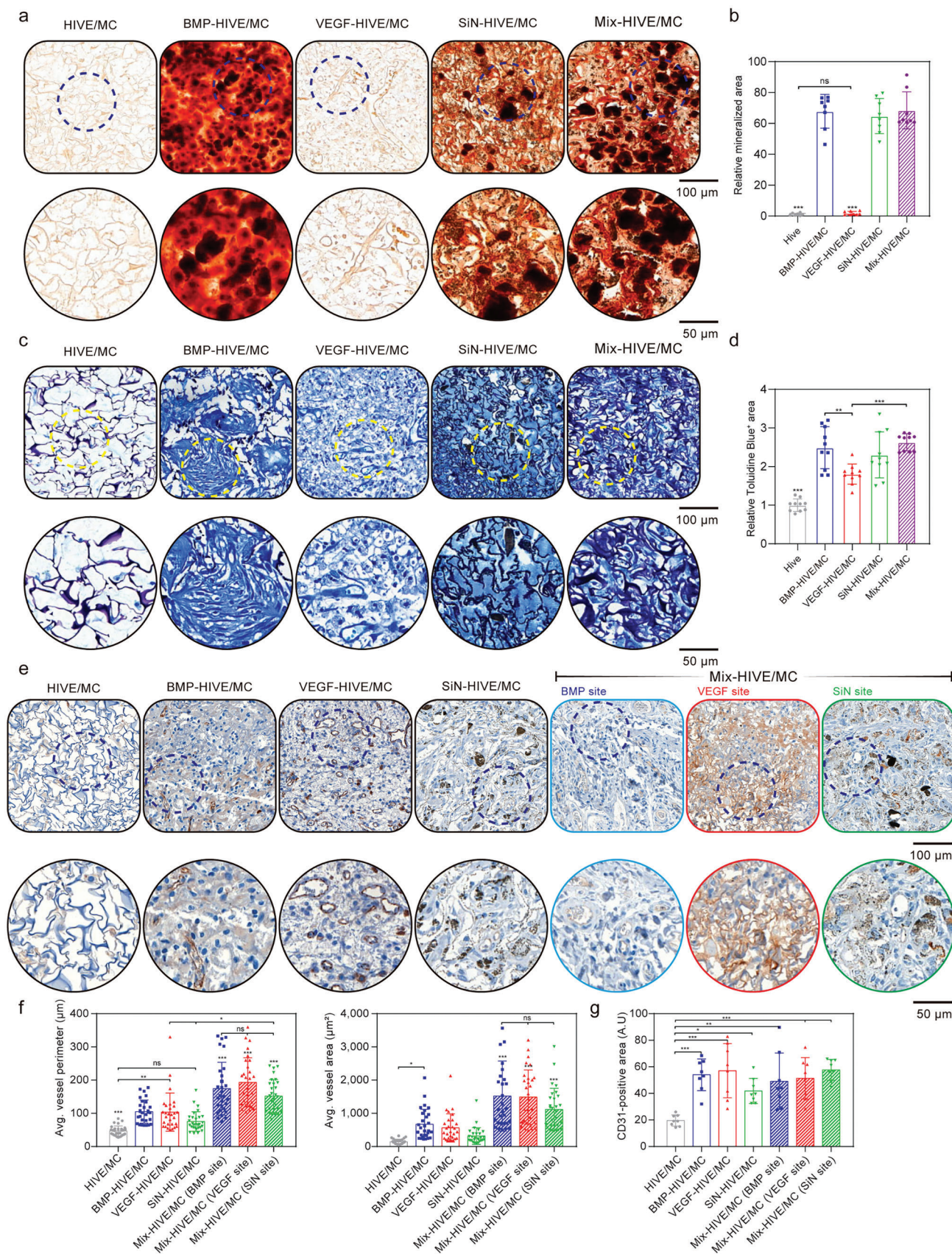
3. Discussion

In this study, we developed a hive-structured assemblable bespoke scaffold (HIVE) system which can be manually assembled to fit any defect and can have site-specific treatments by working as a carrier filled with MCs incorporating different biological factors (Figure 1). The HIVE/MC system is composed of two main components which are HIVE and MC. First, HIVE is a DLP 3D-printed scaffold that can function as an exoskeleton of the whole HIVE/MC and enable assembly in any shape or size. The design of the HIVE is inspired by the honeycomb and its hexagon shape which is efficient at supporting structural loads[13] (Figure 2a). The triangular honeycomb structure, HIVE's unique feature, is known to possess higher mechanical stiffness and strength over various mechanical loading conditions compared to other shapes.[13,14] Furthermore, the shape of the hexagon in HIVE allows for the largest space with the least perimeter, which makes it possible to have a highly porous structure and maximized space to put MCs in the pockets.[14] Its complex structure would increase the overall surface area of the scaffold to help induce more apatite deposition and protein adsorption for bone formation in a physiological system.[6c,12a] Additionally, HIVEs were consistently well-printed, with consistent assemblable forms, and incorporating the desired porous structures that are interconnected without any major defects (Figures 2b). This interconnected macroporous structure of HIVE can provide a beneficial cellular environment for tissue healing by promoting cell infiltration, efficient nutrient flow, and vascular ingrowth[8b,15] (Figure 2c).

MC, the second main component of HIVE, is a type of hydrogel fabricated by cryogelation with EDC/NHS-mediated crosslinking reaction to form an amide group between amine and carboxyl groups from gelatin and heparin.[8b] From many studies, it has been confirmed that cryogels can provide not only a beneficial cellular environment by biocompatibility and hydrophilicity but also through the interconnected macroporous structure.[1d,8] However, since it is composed of a low-concentration solution, its mechanical stiffness is relatively low, a known limitation of such hydrogels, which makes it unfavorable for osteogenic differentiation.[8a,11b] Especially, the stiffness of an implant induces cells to differentiate into the targeted tissue, with a stiffness similar to the scaffold by stimulating cell focal adhesion and signaling.[16] Furthermore, its low mechanical stiffness is not appropriate for use as a standalone implant, which is required to withstand dynamic physiological loading. In order to overcome this drawback, the HIVE was utilized to provide an exoskeleton that can bear the loading and provide mechanical stability as an implant. The mechanical stability of HIVE was evaluated in this study by compressive mechanical testing and FEA. Note that the stiffness of MC was negligible compared to the HIVE, so the main purpose of evaluating the mechanical properties of HIVE/MC was to check the mechanical stability of HIVE.[8a] Overall results confirmed that both single and assembled HIVE scaffolds showed appropriate mechanical properties for use as a bone implant without any brittle fracture (Figure 2d–g). This is beneficial in terms of mechanical stability. Particularly, there have been only a few studies in regenerative medicine evaluating assemblable scaffolds, and the ones that were developed have mechanical limits. For instance, Xia et al. were able to demonstrate PLGA-based microgels to assemble into microtissue by using a Michael addition reaction.[7b] However, both single units and assembled units are made of hydrogels which makes it mechanically unstable against physiological loading levels. Moreover, Subbiah et al. developed a 3D-printed beta-tricalcium phosphate ceramic-based scaffold that can be assembled and shows stronger compressive strength compared to that of mandibular bone.[7a] They explored advanced treatment options by suggesting different therapeutic approaches. However, in their study, in the case of assembly, the strength of two assembled scaffolds was 75% lower than that of a single scaffold. In our study, even in the case of assemblies, there were no significant stress concentrations found at the interface between scaffolds, highlighting that the stability and safety of the implant and the structural properties are not significantly altered by the assembly. In addition, the predicted maximum von Mises stress of the assemblies is comparable to those in the single scaffolds.

Regarding the potential of HIVE/MC as a carrier system for several biological factors, we mainly focused on three applications using HIVE/MC: growth-factor- (BMP and VEGF), bioceramic- (HAP and SiN), and cell- (HUVEC) carriers. Since each biological factor has different effects and characteristics, HIVE/MC allows the users to choose specific effects that users

Figure 6. In vivo tissue formation and cell migration of the HIVE in a rat subcutaneous implantation. a) Scheme of in vivo 4-week rat subcutaneous implantation model that was implanted with HIVE/MC. b) Photographs of HIVE/MC scaffolds that were explanted 4 weeks after the surgery. c,d) Representative cross-section photographs of explanted HIVE/MC stained by H&E (c) and MTC (d) staining. Circular images below are magnified images of the yellow (c) or blue (d) dashed line areas. e) Representative images of multiple locations within HIVE/MC stained by H&E staining. Each magnified image represents the area of dashed line circles. The white dashed lines in the images represent the interface between the MC and HIVE.

© 2023 The Authors. Advanced Materials published by Wiley-VCH GmbH

**ADVANCED
SCIENCE NEWS**

www.advancedsciencenews.com

**ADVANCED
MATERIALS**

www.advmat.de

are aiming for. As a GF carrier, HIVE/MC demonstrated sustained release of BMP-2 and VEGF which play a significant role in bone regeneration (Figure 3c,d). Despite the macroporous structure of MC and HIVE/MC, the controlled drug release feature of HIVE/MC was possible mainly due to the binding affinity of heparin to BMPs and VEGFs.[1d,8b,17] As a result, the ELISA results with BMP-2 and VEGF demonstrated a slower release rate in the HIVE/MC compared to that of HIVE/MC with FITC-BSA, for which heparin does not have an associated binding site. This led to the result that higher calcium deposition and osteogenesis were observed as the number of BMP-loaded MCs increased in HIVE/MC (Figure 3e,i). Furthermore, H+MC1 presented significantly higher ALP activity and mineralization compared to the blank HIVE which suggests even a single BMP-2-loaded MC in HIVE was already effective enough to induce osteogenic effect on hMSCs due to efficient release of BMP-2. These results were consistent with results from other studies developing BMP-eluting scaffolds, that the sustained release of BMP-2 is effective for bone formation.[1d,18] Moreover, sustained release kinetics can also overcome the biggest drawback of BMP-2 which is possible ectopic bone formation in the case of burst release of BMP-2.[18b,19] For instance, Howard et al. fabricated laponite-incorporated layer-by-layer film which can modulate the release kinetics of BMP-2.[20] A sustained release was confirmed with this film, which led to significantly higher bone formation than the control group with burst release in an in vivo rat cranial defect model. Also, in the study of Zhuang et al., heparin-polylactic acid (PLA) based-core/alginate-based-shell microspheres loaded with BMP-2 were developed and combined with a 3D-printed PCL scaffold to have a sustained BMP-2 releasing system for bone repair.[21] In this respect, the HIVE/MC as a BMP-2 carrier system would be constructive and effective, especially for the long-term tissue remodeling phase after the critical defect repair, which is responsible for ECM modeling and bone formation.[22]

With the same motif, we evaluated the angiogenic response of HUVECs on HIVE/MC as a VEGF carrier system. VEGF is another essential GF that can hugely influence bone formation in the physiological system. Especially, right after the inflammation phase, VEGF can induce neovascularization for easier recruitment of stem cells and mineralizing components to defect sites.[11b,23] In our previous studies, we have confirmed in vitro and in vivo angiogenesis and cell migrations of VEGF-loaded gelatin/heparin cryogel by using sustained VEGF release kinetics.[1d,8b] Likewise, our study demonstrated a successful angiogenic effect from HIVE/MC and faster wound healing and tube formation from the HIVE/MC with more VEGF-loaded MCs (Figure 3j–m). Especially, both H+MC3 and H+MC6 groups showed upregulation of angiogenic gene expressions which suggests that three MCs would be efficient enough to induce in vitro angiogenesis and wound healing (Figure 3n). These results were confirmed by many other studies about enhanced tissue formation from the sustained release of VEGF. For example, Li et al.

fabricated a VEGF-loaded collagen hydrogel/porous titanium alloy scaffold which showed successful in vitro tube formation, wound healing angiogenic gene upregulation, and in vivo bone formation due to sustained release of VEGF.[24] Also, Wu et al. used an electrospinning technique to design VEGF encapsulated hyaluronan/PLA/collagen-based microsol membranes that can release VEGF in a sustained manner to induce both angiogenic and osteogenic effects for periosteal regeneration.[25] Note that, in the study, unlike experiments with BMP-2, although H+MC1 showed distinct differences compared to blank HIVE in tube formation and the wound healing assay, a significant angiogenic effect from H+MC1 was not observed in RT-qPCR. This could be due to the insufficient VEGF dose from one MC on HUVECs, thus further in vivo studies will be needed to define the correct amount of VEGF from each HIVE/MC group to be effective. Davies et al. confirmed that the concentration of VEGF plays a significant role in angiogenesis by showing an elevated level of vascularization in a polyurethane scaffold with higher doses of VEGF.[26]

The next HIVE/MC application we focused on was a bioceramic carrier system. We chose two bioceramics to reinforce the MCs: 1) HAP, a widely-known calcium phosphate that has biocompatibility and osteoconductivity 2) SiN, a relatively new synthetic ceramic that also has osteoconductivity and anti-bacterial effect.[6c,11a,27] Both HIVE/MC with HAP or SiN reinforced MC showed high calcium depositions and osteogenic gene upregulations, however, the degree of osteogenesis was different between the groups in early phase (day 7) and later phase (day 14). In the case of ARS, HIVE/MC with HAP groups (HAP group) demonstrated significantly higher calcium deposition than HIVE/MC with SiN groups (SiN group) (Figure 4d,e). However, the gap between the HAP group and the SiN group got smaller on day 14 compared to that on day 7. This could be explained by the abundance of calcium that is already present in HAP, a main inorganic component of human bone. So for HAP groups, it would be easier for ARS to bind to the calcium to form a Lake pigment that is red in color.[28] Thus, the RT-qPCR demonstrated slightly different results than the ARS results. H+MC6 (SiN) showed the highest upregulations in osteogenic gene markers like *ALP* and *COL1* on day 7, suggesting superior early-phase osteogenic effects compared to H+MC6 (HAP) (Figure 4f). However, on day 14, H+MC6 (HAP) exhibited the highest osteogenic gene expressions, indicating greater later-phase osteogenic effects. This could be due to the osteoconductivity of SiN which requires cells to be in contact with material surface for osteogenesis.[29] Meanwhile, although HAP has inferior osteoinductivity compared to other calcium phosphate like β-TCP due to the slow degradation of HAP, its limited osteoinductivity was enough to allow the recruitment of hMSCs and enhanced osteogenic differentiation in this in vitro study.[6c,29a] Other than the osteoinductivity or osteoconductivity from bioceramics itself, there is one more factor that induced osteogenic differentiation which is the higher stiffness

Figure 7. In vivo bone formation and vascularization within the HIVE in a rat subcutaneous implantation. a–d) Representative cross-section photographs of explanted HIVE/MC stained by ARS (a) and toluidine blue (c) staining to demonstrate bone formation. Circular images below are magnified images of the blue (a) or yellow (c) dashed line area. b,d) Quantitative analysis that shows relative mineralized area by ARS (b) and relative toluidine-blue-positive area (d). e) Representative cross-section photographs of explanted HIVE/MC stained by CD31 staining to demonstrate vascularization. The circular images below are magnified images of the blue dashed line area. f) Average perimeter and area of the vessels formed and g) CD31-positive area within the implants. The error bars indicate SD.

**ADVANCED
SCIENCE NEWS**

www.advancedsciencenews.com

**ADVANCED
MATERIALS**

www.advmat.de

of MC due to reinforcement of HAP or SiN. Since the stiffness of the scaffold affects the cell signaling and focal adhesions that would lead cells to differentiate into a tissue that has a similar stiffness to the scaffold, the soft scaffold like hydrogel does not have an ideal stiffness for osteogenic differentiation.[6c,8a,16b,c,30] Instead, scaffolds with higher stiffness like HAP or SiN-loaded MCs are more likely to induce osteogenic differentiation.[11a,31] Furthermore, bioceramic-loaded MCs would provide enhanced mechanical support for the defect area as well as the physiological system.[16d]

Then, we confirmed the potential of HIVE/MC as a cell delivery system by coculturing HUVECs and hMSCs. Since both hMSCs and HUVECs play essential roles in bone regeneration, there were many studies investigating the biological effects of coculture. Generally, it has been reported that coculture of hMSCs and HUVECs can enhance osteogenesis of hMSC by cytokines and regulatory molecules from HUVEC that were induced by the paracrine effects and direct cell-to-cell interactions.[32] For instance, Kim et al. demonstrated that coculturing hMSCs with HUVECs on a nanotopographical substrate enhanced the osteogenesis of hMSC more than culturing hMSC alone on the same substrate.[32a] Also, Guerrero et al. showed that the coculturing hMSC and progenitor-derived endothelial cells on 3D polysaccharide-based porous scaffolds resulted in higher osteogenesis of hMSC. Along with other previous research, this study using HIVE/MC as a HUVEC carrier confirmed higher calcium deposition, angiogenesis, and osteogenesis of hMSCs (Figure 4h–j). Even in the early phase, there were distinct upregulations of some osteogenic genes between H+MC1 and blank HIVE which suggests that HUVECs in single MC have influenced osteogenesis by cell-to-cell signaling and pathway. Interestingly, despite the different numbers of MC in groups, there were fewer differences in gene expression between HIVE/MC groups in a later phase. This emphasizes that unlike GF or bioceramics in MC which is limited, HUVECs in MC were able to proliferate themselves to have osteogenic and angiogenic effects on hMSCs even if the experiment started with fewer MCs.

Then, we confirmed the positive biological effects of the Mix-HIVE/MC group on hMSCs and suggested another new potential with multifunctional and site-specific effects. Mix-HIVE/MC demonstrated the highest calcium deposition and osteogenic differentiation which is mainly due to the synergistic effects of BMP, VEGF, and SiN (Figure 5b,c). There have been many studies about the synergistic effect of bone formation by using both BMP and VEGF.[1d,23a,33] For instance, Wang et al. developed electrospun nanofibrous scaffolds incorporating VEGF, BMP-2, and CaP nanoparticles to recreate ECM-like microstructures with angiogenic and osteogenic properties.[33a] Also, Kempen et al. fabricated a composite consisting of poly(lactic-co-glycolic acid) (PLGA) microspheres loaded with BMP-2 embedded in a poly(propylene) (PPF) scaffold surrounded by a gelatin hydrogel loaded with VEGF to control the release of growth factors for bone regeneration.[23a] However, there is scarce data on SiN for tissue engineering since it has been used only recently in the medical field. To the best of our knowledge, there has not been a study of scaffolds using SiN with other growth factors. Thus, this data from Mix-HIVE/MC highlights that SiN can provide a further synergistic effect for bone formation by combining with BMP and VEGF. Additionally, it emphasizes another potential of multifunctional HIVE/MC which can be used for critical defect sites specifically where rapid bone regeneration is needed. Furthermore, Mix-HIVE/MC successfully demonstrated site-specific effects on the microscale. Each three isolated sites (BMP-, VEGF-, and SiN-sites) from Mix-HIVE/MC represented a different level of osteogenesis (Figure 5d,e). The SiN-site exhibited a high level of osteogenesis, as the BMP-site did, which was different from the result when comparing SiN-HIVE/MC, the HIVE/MC group with only SiN-loaded MCs, to BMP-HIVE/MC. This indicates that the hMSCs on SiN sites were influenced by released BMP and VEGF from BMP/VEGF- sites while the other sites were not affected by the SiN due to osteoconductivity that requires cells to be in contact with the surface of SiN. Despite the influence from other sites, three sites exhibited different gene expressions which allows users to achieve the site-specific effect that they target.

Based on CLSM images, we also confirmed successful cell attachment and migrations even in the case of assemblies. Cells were well attached and spread on both HIVE and MCs filling any gaps in spaces (Figure 5f). Additionally, in the case of assembled HIVE/MC, cells were migrating successfully to acellular HIVE/MC via not only the outer surface (Figure 5i) but also the inner surfaces and inner pores of the scaffold (Figure 5h). These cells on the inner and outer surfaces will be able to have a continuous cell–cell interaction and initiate faster bone formation in all three spatial directions including inside and outside. , the interconnected porous structure of HIVE/MC will ensure sufficient nutrient and oxygen inflow to cells which will improve proliferation, vascularization, and bone ingrowth, as previously shown for other microporous scaffolds.[34]

Finally, we evaluated the in vivo biocompatibility and osteogenic and angiogenic effects of HIVE/MC. In the in vivo subcutaneous implantation, all groups including HIVE/MC, a control group, were able to exhibit successful cell migration, because the MCs support the migration of host cells due to its macroporous and interconnected structure, providing a biocompatible microenvironment for cell proliferation and host cell infiltration into the scaffold upon implantation (Figure 6).[35] Additionally, despite some differences among the groups, all groups presented a certain level of collagen tissue formation and angiogenesis within the scaffolds (Figure 6 and Figure 7). These show consistent results with other studies as well. For instance, Kim et al. demonstrated that the macroporous structure of cryogel enabled cell migration and neovascularization into the scaffold in an in vivo mouse ischemic hind limb model.[8b] Also, Bloch et al., confirmed new blood vessel formation and endothelial cells in subcutaneously implanted agarose-gelatin-based cryogel that they developed.[36] Moreover, although the implantation was conducted using a subcutaneous model, mineralization and formation of proteoglycan and GAGs within HIVE systems were observed especially in the groups (BMP-, SiN-, and Mix-HIVE/MC) (Figure 7a,c). It should be noted that VEGF-HIVE/MC demonstrated minimal mineralization compared to the other groups. However, it exhibited a certain level of toluidine-blue-positive area, suggesting that the angiogenic effect of VEGF indirectly supported the formation of proteoglycans and GAGs, which could aid in bone formation. Along with the positive biological effects from MC, HIVE's unique open- and interconnected-porous structure ensured cell migration and tissue formation into the whole scaffold (Figure 6e). In a

**ADVANCED
SCIENCE NEWS**

www.advancedsciencenews.com

**ADVANCED
MATERIALS**

www.advmat.de

physiological system, this structure would promote a more stable fixation of the assembly and better osseointegration with the host bone due to interlocking between the scaffold surface and the surrounding tissue.[37] Furthermore, we confirmed that the sustained release of BMP or VEGF and incorporation of SiN in the scaffold was effective to induce distinct in vivo tissue formation and vascularization (Figure 6c,d and Figure 7a,e). Especially, the Mix-HIVE/MC demonstrated not only a synergistic effect of BMP, VEGF, and SiN to induce the highest tissue formation with vascularization among the groups but also site-specific effects in each pocket. There have been many studies that show the combined effect of growth factors and bioceramics like hydroxyapatite.[38] For example, Chen et al. developed a BMP-2 and VEGF-loaded 3D-printed hydroxyapatite/gelatin/chitosan composite scaffold which resulted in enhanced osteogenic and angiogenic effect in an in vivo rabbit calvarial defect model.[38b] However, it is not possible for those scaffolds to have precisely controlled site-specific effects at the targeted area like Mix-HIVE/MC.

To the best of our knowledge, this is the first study that evaluated a fully assemblable platform that can work as a multifunctional biological factor carrier to achieve both site-specific and patient-specific treatment. There have been some studies previously that showed possible concepts of a site-specific scaffold. For instance, Liu et al. developed PEGDA MCs for site-directed and fibroblast cell delivery and showed successful angiogenesis in a mouse subcutaneous implantation model.[9a] However, the system did not have stable mechanical properties and showed difficult localization at an exact defect area, which are common problems of hydrogel-based scaffolds as cell delivery systems.[39] In other studies, assemblable scaffolds were fabricated, such as cylindrical pin and hole structured titanium scaffolds, that can be stacked in a two-body combination.[40] However, the scaffolds had limited assembly configurations, and cannot work as a carrier for cell or growth factors for enhanced treatment. Furthermore, the final scaffold did not have an interconnected porous structure which made it difficult to have efficient cell infiltration and bone ingrowth. However, in the case of HIVE/MC, there are many aspects that can be customized for surgeons to control the tissue formation rate at a specific region in the defect by choosing specific cell/growth factor/bioceramic-loaded MCs. The main advantage of HIVE/MC would be unlimited combinations of the HIVE assembly, so with multifunctional MCs, numerous developments based on HIVE/MC can be achieved for more precise patient-specific and site-specific tissue regeneration.

4. Experimental Section

3D Printing of HIVE Scaffold: The overall structure of HIVE was designed with Fusion 360 (Autodesk), and for the 3D printing of HIVE, the slicer software PrusaSlicer (version 2.3.3+x64, Prusa Research) and a commercially available DLP 3D printer (Ember, Autodesk) were used for print file generation and 3D printing, respectively. For the printing material, a commercially available biocompatible resin (Biotough D80 MF Monomer Free, P10154, 3Dresyns) was used. First, a Petri dish was covered with a fluorinated ethylene propylene film (McMaster Carr) in order to minimize the adhesion of the printed part. Then, ≈10 mL of resin was filled in the coated Petri dish before the 3D printing. The settings for the printer

were: first exposure 3 s, burn-in layers 4, burn-in exposure 1 s, model exposure 0.7 s, Z-lift 750 µm and layer thickness 25 µm. After printing, the HIVE was thoroughly rinsed in isopropanol to remove the remaining resin.

Fabrication of Microcryogel (MC):   MC was polymerized via an EDC/NHS crosslinking reaction as described in a previous study.[1d,8] Briefly, 1% (w/v) of type A gelatin (G1890, Sigma-Aldrich) and 0.3% (w/v) of heparin (Merck Millipore, 375 095) were dissolved in distilled water. Then, 50 mM of EDC (PG82079, Thermo Scientific) and 25 mM of sulfo-NHS (PG82071, Thermo Scientific) in distilled water were added to the gelatin/heparin mixed solution. After that, 10 µL of mixed precursor solution was pipetted into pre-cooled parafilm-based molds, and the molds were placed in −a 20 °C refrigerator overnight to induce cryogelation. After cryogelation, MCs were lyophilized for a minimum of 4 h to remove ice crystals. After lyophilization, MCs were soaked and fully swollen with PBS until used in further experiments. For MC loading in the HIVE scaffold, each MC was picked up by the atraumatic tweezers and gently put in each pocket of the HIVE.

For the bioceramic reinforced MC, MCs were loaded with hydroxyapatites or silicon nitride as described in the previous study.[11a] Briefly, hydroxyapatite nanopowders (HAP) (677418-10G, Sigma-Aldrich) or silicon nitride microparticles (SiN) (MC2 Silicon Nitride, SINTX Technologies, USA) were dispersed in distilled water (DW) homogenously to obtain 20% (w/v) of HAP or SiN solution. Then, 10 MCs were put in 1 mL of HAP or SiN solution in a microtube and vortexed at 1400 RPM for 2 h in a Thermomixer (Eppendorf, Thermomixer). After vortexing, bioceramic reinforced MCs were dipped in clean DW and vortexed at 500 RPM for 1 h to wash out extra bioceramic particles on the surface of the MC. For sterilization for in vitro experiments, MCs were soaked with PBS and sterilized by UV irradiation for 3 h.

Mechanical Test: The single HIVE scaffolds were tested using a materials testing machine (Instron E10000, Instron, UK) at a displacement speed of 0.01 mm s^{-1} under compression. Also, to investigate the mechanical strength of the HIVE system in assembled configurations, compression tests were performed using assembled configurations of the scaffolds under axial and lateral loading, respectively. Between two parallel smooth plates, an unconfined quasi-static compression was performed, and the displacement and force were recorded continuously throughout the experiment. To investigate the durability of the HVIE, two different cyclic loading protocols were applied at a constant displacement rate of 0.01 mm s^{-1}: cyclic loading to a predefined maximum strain (8%) at each loading cycle, and progressive loading to a maximum strain (10%) in increasing steps, with full unloading in between loading steps.

Finite Element Analysis (FEA):   The mechanical strength of the HIVE was demonstrated with FEA under different loading conditions. The material, Biotough D80 Monomer Free, was assumed to be isotropic and linear elastic with a Poisson ratio of 0.4, Young's modulus of 2000 MPa, and flexural strength of 100 MPa. Two load-cases were studied; a pressure of 1.25 MPa, the maximum intradiscal pressure reported in other studies,[10] was applied: 1) on the top surface with the bottom surface fully constrained, and 2) on the side surface with the opposite side of the scaffold fully constrained. A commercial FEM solver (NX 12.0) was used to perform the linear static analysis using a mesh with 10-node tetrahedral elements. The final mesh resolution was determined after conducting a mesh convergence study. The mechanical behavior was inspected by plotting the Von Misses stress.

In addition, to investigate the mechanical strength of the assembled HIVE system, FEA was performed with two or more scaffolds in an assembled configuration. Two complex assembly configurations were studied for load-case 1 named ASSY1 and ASSY2. Where two or more scaffolds were simulated in stacked or assembled configuration the interface between the scaffolds was assumed to be rigidly tied. This assumption was proposed after observing in experiments that the scaffolds were tightly assembled, therefore displacements between the assembled components could be neglected. Furthermore, a triple-stacked configuration resembling a conventional scaffold was simulated. The conventional scaffold had the same structure with similar porosity and topology compared to the HIVE, the assemblable scaffold and consisted of a single part

2302008 (17 of 20)

while HIVE was triple stacked. This configuration was simulated to compare the mechanical stability between the assemblable and conventional scaffold.

Field-Emission Scanning Electron Microscopy (FE-SEM): HIVE scaffolds were fixed at different angles on metal stubs with carbon tape and coated with platinum/palladium (80/20) sputtering (CCU-010, Safematic). Then, FE-SEM (FE-SEM SU5000, Hitachi) was used to capture the printing quality and microstructure of the scaffolds at different positions at 3 kV.

Measurement of Drug Release Kinetics: To investigate the growth factor release difference due to MC in the HIVE system, the drug release kinetics were compared between the blank HIVE and HIVE with 6 MC (H+MC6). 30 µL (for blank HIVE) or 5 µL (for each MC in H+MC6) of 0.01% (w/v) fluorescein isothiocyanate conjugated bovine serum albumin (FITC-BSA; A9771, Sigma-Aldrich), 100 ng mL^{-1} VEGF (100-20, Peprotech) or 100 ng mL^{-1} BMP-2 (120-02, Peprotech) was loaded into blank HIVE or each MC for H+MC6. In detail, for the H+MC6 group, the proteins were soaked to each MC that were dehydrated by gently tapping on sterilized gauze. Then, each MC was loaded in the pockets of HIVE with a sterilized tweezer. For the blank HIVE group, the proteins were loaded on the center of each pocket of HIVE to initiate physical adsorption. After 10 min to bind proteins to the scaffold, the samples were each submerged in 500 µL of PBS and PBS was collected at each time point. For FITC-BSA release kinetics, the released amount from collected PBS at each time point was measured by fluorescence spectroscopy (Infinite 200 Pro microreader, Tecan) at an excitation wavelength of 490 nm, and emission wavelength of 525 nm. For VEGF or BMP-2, the released amount was measured with a VEGF ELISA kit (BGK15692, Peprotech) or a BMP-2 ELISA Kit (BGK8C060, Peprotech) respectively by following the standard protocol. The number of replicates used in these experiments was three.

Cell Culture: Human mesenchymal stem cells (hMSCs, P3 and P4, human bone marrow) were obtained from the University of Zurich, Zurich, Switzerland, and human umbilical vein endothelial cells (HUVECs, P2, and P3; C-12203, Sigma-Aldrich) were purchased. For hMSC, cells were cultured in growth medium (GM) composed of MEM α without ascorbic acid (A1049001, Thermofisher), 10% fetal bovine serum (26 140 079, Thermofisher) and 1% antibiotic–antimycotic (15240062, Thermofisher). For HUVECs, cells were cultured in a HUVEC growth medium with a supplement mix kit (C-22010, Sigma-Aldrich).

Cell Attachment and Migration: Actin and cell nuclei were stained with Alexa Fluor 568 Phalloidin (A12380, Thermofisher) and DAPI (62 247, Thermofisher) by following the standard protocol. Briefly, after culturing, hMSCs or HUVECs cultured on scaffolds were washed with PBS and fixed in 4% PFA in PBS for 15 min. Then, cells were rinsed three times with PBS and permeabilized using 0.1% Triton X-100 in PBS for 15 min and blocked with a 0.1% Triton X-100 in PBS solution with 1% BSA (A2153, Sigma-Aldrich) for 45 min. For actin staining, cells on scaffolds were stained with fluorescent phalloidin staining solution for 60 min, and the samples were rinsed at least three times with PBS. For DAPI staining, the scaffolds were stained with the DAPI working solution for 5 min and rinsed with PBS to remove excess staining solution. After staining, the samples were visualized with confocal laser scanning microscopy (880 air scan, Zeiss). In the case of observation for cell migration in assembled HIVE scaffolds, first, the cells were seeded onto a single HIVE scaffold. After 3 h of attachment, cells were cultured with GM for 3 days. Then, the cell-laden HIVE was assembled with another clean acellular HIVE scaffold, and the assembled scaffolds were cultured with GM for 1 week. Finally, the actin and nuclei of cells on assembled scaffolds were stained with phalloidin and DAPI staining in the same manner to observe the cell migration between HIVE scaffolds.

HUVEC Tube Formation and Wound-Healing Assay: HUVECs (P2) were cultured with HUVEC GM in the presence of HIVE groups prior to the experiments. For tube formation assay, first, 200 µL of matrigel (354 234, Corning) in ice was pipetted to a precooled 48-well plate and incubated for 30 min at 37 °C. Then, 3×10^5 VEGF-primed HUVECs were seeded onto the matrigel in the wellplate and cultured with HUVEC GM for 10 h. After 6 and 10 h of incubation, images of cells were taken using a light microscope (DP74, Olympus). In addition, at 10 h of incubation, cells were stained for 10 min in 0.5 µL mL^{-1} calcein-AM from the Live/Dead assay kit

(L3224, Thermofisher) and visualized by fluorescence microscopy (LX51, Olympus) for further analysis.

For the wound-healing assay, first, 1×10^4 HUVECs were seeded on a gelatin-coated 24-well plate, and cells were cultured with conditioned GM. When the cells were confluent, the cells were scratched in a straight line with a 1000 µl pipet tip to make a vertical empty space. Then, the cells were washed with PBS and cultured with HUVEC GM for 24 h. After 24 h, the cells were fixed in 4% PFA for 10 min, stained with DAPI, and measured its wound healing rate by fluorescence microscopy. The number of replicates used in these experiments was three.

In Vitro Osteogenic Differentiation: First, OM for hMSC was prepared by adding 100 nM of dexamethasone (D4902, Sigma-Aldrich), 10 mM of glycerol-2-phosphate disodium salt hydrate (G9422, Sigma-Aldrich), and 50 µg mL^{-1} of L-ascorbic acid (A92902, Sigma-Aldrich) in GM. After seeding hMSCs on the scaffolds, and cells were cultured with GM for cell attachment for one day and changed to OM for osteogenic differentiation. OM was changed every two days, and ALP staining, ARS staining, and RT-qPCR were performed to evaluate the osteogenic differentiation of the samples.

ALP and ARS Staining: ALP staining was performed on the cell-laden scaffolds after 7 days of culturing with OM. After 7 days of osteogenic induction, an ALP kit (Sigma-Aldrich, 85L-2) was utilized for staining by following the standard protocol. For ARS staining, it was performed on samples after 7 and 14 days of osteogenic induction by using an ARS kit (0223, Sciencell Research). Briefly, cells on scaffolds were fixed in 4% PFA (281 692, Santa Cruz Biotech) for 15 min and washed three times with DW. Then, the samples were stained with ARS solution for 30 min and washed with distilled water until excess staining solutions were rinsed. After staining, the images of stained cells were taken using a light microscope. Then, the amount of mineral deposited on samples was measured by eluting the ARS with 10% cetylpyridinium chloride (C0732, Sigma-Aldrich), and the optical density of the eluted solution was measured at OD 570 nm using the microplate reader (Infinite 200 Pro, Tecan Life Sciences). The number of replicates used in this experiment was three.

Real-Time Quantitative PCR (RT-qPCR) Analysis: The total RNA of hMSCs or HUVECs in the experiments was extracted by RNeasy Plus Mini Kit (Qiagen Inc., USA). RT-qPCR was performed to confirm osteogenic or angiogenic gene expression levels by using TaqMan gene expression assays with the following probe/primer combinations: *GAPDH*, Hs02786624_g1; *ALP*, Hs01029144_m1; *COL1*, Hs00164004_m1; *RUNX2*, Hs01047973_m1; *OCN*, Hs01587814_g1; *KDR*, Hs00911700_m1; *FGF2*, Hs00266645_m1; *VEGF*, Hs00900055_m1; *HIF1A*, Hs00153153_m1; (ThermoFisher Scientific, USA). The number of replicates used in this experiment was three.

In Vivo Rat Subcutaneous Implantation Model: All experiments were carried out following the Animal Welfare Act, Animal Welfare Ordinance, and Animal Experimentation Ordinance by ETH Zurich and Kanton Zurich (Approval No. ZH035/2022). Female, 8-week-old 35 Wistar rats (Charles River) were utilized for the development of in vivo rat subcutaneous implantation model. All rats were housed in cages at least one week before the surgery and were handled in climate-controlled rooms with 12 h light/dark cycles. Analgesia (Tramadol, 25 mg L^{-1}) was provided via drinking water during the peri-operative period (two days before surgery until the third postoperative day). Anesthesia was induced in a plexiglas box with 5% isoflurane in 100% oxygen, flow rate 1 L min^{-1}. When the animal was asleep, eye cream was applied to prevent desiccation of the cornea, and anesthesia was continued with 1.5% isoflurane in 100% oxygen for surgery. After anesthesia, animals were positioned prone to provide better oxygenation on the heating pad to keep warm. After shaving the surgical region with an electric clipper and sterilizing the skin with povidone–iodine, a 20 mm dorsal midline incision was made over the thoracolumbar area. The skin was held with atraumatic forceps and two subcutaneous pockets were formed bilaterally by blunt preparation with forceps. Five different groups were defined, with samples placed in each subcutaneous pocket: Hive group: negative control, which was a Hive scaffold with blank 6 MCs, BMP-HIVE/MC group: HIVE/MC with 6 BMP-loaded MCs, VEGF-HIVE/MC group: HIVE/MC with 6 VEGF-loaded MCs, SiN-HIVE/MC group: HIVE/MC with 6 SiN reinforced MCs and Mix-HIVE/MC

group: HIVE/MC with 2 BMP-loaded MCs, 2 VEGF-loaded MCs and 2 SiN reinforced MCs. The concentration of BMP and VEGF that used in vivo was both 500 ng mL^{-1}. Then, the incision was closed using staples. After surgery, the animals were directly monitored while awakening from anesthesia and were placed back to their ranks once the animals started moving around again. Staples were removed 10 days after surgery. After 4 weeks of subcutaneous implantation, implanted scaffolds were harvested after the animals were anesthetized and euthanized.

In Vivo Histology: For immunohistochemistry and conventional histological analysis, the harvested scaffolds were fixed in 4% buffered formalin overnight. After fixation, some scaffolds were cut and dehydrated through a series of ascending alcohol concentrations, defatted in xylene, embedded in paraffin, and cast into blocks. The cut scaffolds were positioned both vertically and horizontally in the blocks so that sections would reveal structures both along the circular plane of the scaffolds and across the scaffold height. A Leica RM2235 microtome (Leica Microsystems GmbH, Wetzlar, Germany) was used to cut the blocks into 2–4 µm paraffin slides. Slides were stained with hematoxylin and eosin (H&E), Masson's trichrome, ARS, and toluidine blue staining.

CD31 Immunohistochemistry: A heat-mediated antigen retrieval was conducted (PT-Link, 97 °C, 20 min, in Tris-EDTA Buffer, pH 9.0). Subsequently, the sections were immunolabeled with a primary antibody recognizing CD31 (ab28364, Abcam, dilution 1:50) for 1 h at room temperature. A secondary anti-mouse/rabbit IgG (Dako EnVision+ Dual Link System-HRP) was applied for 30 min at room temperature, followed by the 3,3′-diaminobenzidine (DAB) substrate kit (Dako) as a chromogen. Finally, the sections were counter-stained with Gill's hematoxylin for 20 s.

Statistical Analysis: All experiments were performed at least in triplicate and all data were analyzed as mean $\pm$ standard deviation (SD). For statistical analysis, one-way analysis of variance (ANOVA) was performed followed by Tukey's post hoc test, and statistical significance was considered by *p*-value: *$p < 0.05$, **$p < 0.01$, and ***$p < 0.005$. GraphPad Prism was used for statistical analysis.

Supporting Information

Supporting Information is available from the Wiley Online Library or from the author.

Conflict of Interest

The authors declare no conflict of interest.

Data Availability Statement

The data that support the findings of this study are available from the corresponding author upon reasonable request.

[1] a) T. Gong, J. Xie, J. Liao, T. Zhang, S. Lin, Y. Lin, *Bone Res.* **2015**, *3*, 15029; b) A. Longoni, L. Knežević, K. Schepers, H. Weinans, A. J. W. P. Rosenberg, D. Gawlitta, *npj Regen. Med.* **2018**, *3*, 22; c) S. Amirthalingam, S. S. Lee, M. Pandian, J. R., S. Iyer, N. Hwang, R. Jayakumar, *Biomater. Sci.* **2021**, *9*, 2439; d) S. S. Lee, J. H. Kim, J. Jeong, S. H. L. Kim, R. H. Koh, I. Kim, S. Bae, H. Lee, N. S. Hwang, *Biomaterials* **2020**, *257*, 120223.

[2] a) N. Kleger, M. Cihova, K. Masania, A. R. Studart, J. F. Löffler, *Adv. Mater.* **2019**, *31*, 1903783; b) Z. Lin, M. Wu, H. He, Q. Liang, C. Hu, Z. Zeng, D. Cheng, G. Wang, D. Chen, H. Pan, C. Ruan, *Adv. Funct. Mater.* **2019**, *29*, 1808439; c) A. E. Jakus, A. L. Rutz, S. W. Jordan, A. Kannan, S. M. Mitchell, C. Yun, K. D. Koube, S. C. Yoo, H. E. Whiteley, C.-P. Richter, R. D. Galiano, W. K. Hsu, S. R. Stock, E. L. Hsu, R. N. Shah, *Sci. Transl. Med.* **2016**, *8*, 358ra127; d) N. Kleger, S. Fehlmann, S. S. Lee, C. Dénéréaz, M. Cihova, N. Paunović, Y. Bao, J.-C. Leroux, S. J. Ferguson, K. Masania, A. R. Studart, *Adv. Mater.* **2022**, *34*, 2203878.

[3] a) N. Yu, T. Nguyen, Y. D. Cho, N. M. Kavanagh, I. Ghassib, W. V. Giannobile, *Orthod. Craniofacial Res.* **2019**, *22*, 69; b) L. Vidal, C. Kampleitner, S. Krissian, M. Á. Brennan, O. Hoffmann, Y. Raymond, Y. Maazouz, M.-P. Ginebra, P. Rosset, P. Layrolle, *Sci. Rep.* **2020**, *10*, 7068.

[4] G. Frija, I. Blažić, D. P. Frush, M. Hierath, M. Kawooya, L. Donoso-Bach, B. Brkljačić, *eClinicalMedicine* **2021**, *38*, 101034.

[5] a) S. Bose, M. Roy, A. Bandyopadhyay, *Trends Biotechnol.* **2012**, *30*, 546; b) S. Amirthalingam, A. Ramesh, S. S. Lee, N. S. Hwang, R. Jayakumar, *ACS Appl. Bio. Mater.* **2018**, *1*, 1037.

[6] a) C. Acevedo, V. A. Stadelmann, D. P. Pioletti, T. Alliston, R. O. Ritchie, *Nat. Biomed. Eng.* **2018**, *2*, 62; b) K. L. Christman, *Science* **2019**, *363*, 340; c) S. S. Lee, X. Du, I. Kim, S. J. Ferguson, *Matter* **2022**, *5*, 2722.

[7] a) R. Subbiah, C. Hipfinger, A. Tahayeri, A. Athirasala, S. Horsophonphong, G. Thrivikraman, C. M. França, D. A. Cunha, A. Mansoorifar, A. Zahariev, J. M. Jones, P. G. Coelho, L. Witek, H. Xie, R. E. Guldberg, L. E. Bertassoni, *Adv. Mater.* **2020**, *32*, 2001736; b) P. Xia, S. Yan, G. Li, J. Yin, *ACS Appl. Mater. Interfaces* **2022**, *14*, 12089; c) S. S. Lee, X. Du, T. Smit, E. G. Bissacco, D. Seiler, M. d. Wild, S. J. Ferguson, *bioRxiv* **2023**, https://doi.org/10.1101/2023.03.30.534953.

[8] a) S. S. Lee, M. Santschi, S. J. Ferguson, *Biomacromolecules* **2021**, *22*, 2460; b) I. Kim, S. S. Lee, S. Bae, H. Lee, N. S. Hwang, *Biomacromolecules* **2018**, *19*, 2257.

[9] a) W. Liu, Y. Li, Y. Zeng, X. Zhang, J. Wang, L. Xie, X. Li, Y. Du, *Acta Biomater.* **2014**, *10*, 1864; b) D. Dyondi, T. J. Webster, R. Banerjee, *Int. J. Nanomed.* **2012**, *8*, 47; c) T. T. N. Vo, F. K. Kasper, A. G. A. Mikos, *Adv. Drug Delivery Rev.* **2012**, *64*, 1292.

[10] M. Dreischarf, A. Shirazi-Adl, N. Arjmand, A. Rohlmann, H. Schmidt, *J. Biomech.* **2016**, *49*, 833.

[11] a) S. S. Lee, L. Laganenka, X. Du, W.-D. Hardt, S. J. Ferguson, *Front. Bioeng. Biotechnol.* **2021**, *9*, 794586; b) I. Kim, S. S. Lee, S. H. L. Kim, S. Bae, H. Lee, N. S. Hwang, *Macromol. Biosci.* **2019**, *19*, 1800460.

[12] a) S. S. Lee, S. Huber, S. J. Ferguson, *Mater. Sci. Eng., C* **2021**, *127*, 112251; b) T. J. Webster, A. A. Patel, M. N. Rahaman, B. S. Bal, *Acta Biomater.* **2012**, *8*, 4447; c) X. Du, S. S. Lee, G. Blugan, S. J. Ferguson, *Int. J. Mol. Sci.* **2022**, *23*, 6551; d) X. Du, G. Blugan, T. Künniger, S. S. Lee, L. Vladislavova, S. J. Ferguson, *Ceram. Int.* **2021**, *47*, 33525.

[13] Q. Zhang, X. Yang, P. Li, G. Huang, S. Feng, C. Shen, B. Han, X. Zhang, F. Jin, F. Xu, T. J. Lu, *Prog. Mater. Sci.* **2015**, *74*, 332.

[14] M. L. Smith, N. Napp, K. H. Petersen, *Proc. Natl. Acad. Sci. USA* **2021**, *118*, e2103605118.

[15] S. A. Bencherif, R. W. Sands, D. Bhatta, P. Arany, C. S. Verbeke, D. A. Edwards, D. J. Mooney, *Proc. Natl. Acad. Sci. USA* **2012**, *109*, 19590.

[16] a) T. Zhang, S. Lin, X. Shao, S. Shi, Q. Zhang, C. Xue, Y. Lin, B. Zhu, X. Cai, *J. Cell. Physiol.* **2018**, *233*, 3418; b) S. H. Oh, D. B. An, T. H. Kim, J. H. Lee, *Acta Biomater.* **2016**, *35*, 23; c) A. J. Engler, S. Sen, H.

**ADVANCED
SCIENCE NEWS**

www.advancedsciencenews.com

**ADVANCED
MATERIALS**

www.advmat.de

L. Sweeney, D. E. Discher, *Cell* **2006**, *126*, 677; d) G. Chen, C. Dong, L. Yang, Y. Lv, *ACS Appl. Mater. Interfaces* **2015**, *7*, 15790.

[17] a) Y. J. Choi, J. Y. Lee, J. H. Park, J. B. Park, J. S. Suh, Y. S. Choi, S. J. Lee, C.-P. Chung, Y. J. Park, *Biomaterials* **2010**, *31*, 7226; b) N. S. Gandhi, R. L. Mancera, *Biochim. Biophys. Acta, Proteins Proteomics* **2012**, *1824*, 1374.

[18] a) J. M. Wozney, *Spine* **2002**, *27*, S2; b) D. H. R. Kempen, L. Lu, T. E. Hefferan, L. B. Creemers, A. Maran, K. L. Classic, W. J. A. Dhert, M. J. Yaszemski, *Biomaterials* **2008**, *29*, 3245; c) X. Shen, Y. Zhang, Y. Gu, Y. Xu, Y. Liu, B. Li, L. Chen, *Biomaterials* **2016**, *106*, 205.

[19] a) J. Wozney, V. Rosen, A. Celeste, L. Mitsock, M. Whitters, R. Kriz, R. Hewick, E. Wang, *Science* **1988**, *242*, 1528; b) Q. Kang, M. H. Sun, H. Cheng, Y. Peng, A. G. Montag, A. T. Deyrup, W. Jiang, H. H. Luu, J. Luo, J. P. Szatkowski, P. Vanichakarn, J. Y. Park, Y. Li, R. C. Haydon, T. C. He, *Gene Ther.* **2004**, *11*, 1312; c) E. A. Wang, V. Rosen, J. S. D'Alessandro, M. Bauduy, P. Cordes, T. Harada, D. I. Israel, R. M. Hewick, K. M. Kerns, P. LaPan, *Proc. Natl. Acad. Sci. USA* **1990**, *87*, 2220.

[20] M. T. Howard, S. Wang, A. G. Berger, J. R. Martin, S. Jalili-Firoozinezhad, R. F. Padera, P. T. Hammond, *Biomaterials* **2022**, *288*, 121721.

[21] W. Zhuang, G. Ye, J. Wu, L. Wang, G. Fang, Z. Ye, G. Lai, X. Qiu, H. Sang, *Biomater. Adv.* **2022**, *133*, 112619.

[22] a) G. Hosgood, *Vet. Clin. North Am.: Small Anim. Pract.* **2006**, *36*, 667; b) T. B. Wissing, V. Bonito, C. V. C. Bouten, A. Smits, *npj Regen. Med.* **2017**, *2*, 18; c) R. J. Bodnar, *Adv. Wound Care* **2015**, *4*, 641.

[23] a) D. H. R. Kempen, L. Lu, A. Heijink, T. E. Hefferan, L. B. Creemers, A. Maran, M. J. Yaszemski, W. J. A. Dhert, *Biomaterials* **2009**, *30*, 2816; b) B. Li, H. Wang, G. Zhou, J. Zhang, X. Su, Z. Huang, Q. Li, Z. Wu, G. Qiu, *RSC Adv.* **2017**, *7*, 4253.

[24] Y. Li, Y. Liu, H. Bai, R. Li, J. Shang, Z. Zhu, L. Zhu, C. Zhu, Z. Che, J. Wang, H. Liu, L. Huang, *Front. Bioeng. Biotechnol.* **2021**, *9*, 757767.

[25] L. Wu, Y. Gu, L. Liu, J. Tang, J. Mao, K. Xi, Z. Jiang, Y. Zhou, Y. Xu, L. Deng, L. Chen, W. Cui, *Biomaterials* **2020**, *227*, 119555.

[26] N. Davies, S. Dobner, D. Bezuidenhout, C. Schmidt, M. Beck, A. H. Zisch, P. Zilla, *Biomaterials* **2008**, *29*, 3531.

[27] K. Zhang, Y. Zhou, C. Xiao, W. Zhao, H. Wu, J. Tang, Z. Li, S. Yu, X. Li, L. Min, Z. Yu, G. Wang, L. Wang, K. Zhang, X. Yang, X. Zhu, C. Tu, X. Zhang, *Sci. Adv.* **2019**, *5*, eaax6946.

[28] D. L. Sterchi, in *Bancroft's Theory and Practice of Histological Techniques (Eighth Edition)*, (Eds: S. K. Suvarna, C. Layton, Eds., J. D. Bancroft), Elsevier, Amsterdam, The Netherlands **2019**.

[29] a) T. Albrektsson, C. Johansson, *Eur. Spine J.* **2001**, *10*, S96; b) G. Pezzotti, R. M. Bock, T. Adachi, A. Rondinella, F. Boschetto, W. Zhu, E. Marin, B. McEntire, B. S. Bal, O. Mazda, *Appl. Mater. Today* **2017**, *9*, 82.

[30] B. V. Slaughter, S. S. Khurshid, O. Z. Fisher, A. Khademhosseini, N. A. Peppas, *Adv. Mater.* **2009**, *21*, 3307.

[31] S. Kwon, S. Lee, A. Sivashanmugam, J. Kwon, S. Kim, M. Noh, S. Kwon, R. Jayakumar, N. Hwang, *Polymers* **2018**, *10*, 914.

[32] a) J. Kim, H. N. Kim, K.-T. Lim, Y. Kim, S. Pandey, P. Garg, Y.-H. Choung, P.-H. Choung, K.-Y. Suh, J. H. Chung, *Biomaterials* **2013**, *34*, 7257; b) J. Ma, J. J. van den Beucken, F. Yang, S. K. Both, F. Z. Cui, J. Pan, J. A. Jansen, *Tissue Eng., Part C* **2011**, *17*, 349; c) G. Gurel Pekozer, G. Torun Kose, V. Hasirci, *Microvasc. Res.* **2016**, *108*, 1; d) J. Guerrero, S. Catros, S. M. Derkaoui, C. Lalande, R. Siadous, R. Bareille, N. Thébaud, L. Bordenave, O. Chassande, C. Le Visage, D. Letourneur, J. Amédée, *Acta Biomater.* **2013**, *9*, 8200.

[33] a) C. Wang, M. Wang, *J. Mater. Chem. B* **2017**, *5*, 1388; b) R. Subbiah, M. P. Hwang, S. Y. Van, S. H. Do, H. Park, K. Lee, S. H. Kim, K. Yun, K. Park, *Adv. Healthcare Mater.* **2015**, *4*, 1982.

[34] a) N. Abbasi, S. Hamlet, R. M. Love, N.-T. Nguyen, *J. Sci.: Adv. Mater. Devices* **2020**, *5*, 1; b) G. Turnbull, J. Clarke, F. Picard, P. Riches, L. Jia, F. Han, B. Li, W. Shu, *Bioact. Mater.* **2018**, *3*, 278; c) A. Samourides, L. Browning, V. Hearnden, B. Chen, *Mater. Sci. Eng., C* **2020**, *108*, 110384.

[35] C. M. Murphy, M. G. Haugh, F. J. O'Brien, *Biomaterials* **2010**, *31*, 461.

[36] K. Bloch, A. Vanichkin, L. G. Damshkaln, V. I. Lozinsky, P. Vardi, *Acta Biomater.* **2010**, *6*, 1200.

[37] a) N. Taniguchi, S. Fujibayashi, M. Takemoto, K. Sasaki, B. Otsuki, T. Nakamura, T. Matsushita, T. Kokubo, S. Matsuda, *Mater. Sci. Eng., C* **2016**, *59*, 690; b) M. De Wild, C. Ghayor, S. Zimmermann, J. Rüegg, F. Nicholls, F. Schuler, T.-H. Chen, F. E. Weber, *3D Print. Addit. Manuf.* **2018**, *6*, 40.

[38] a) V. Fitzpatrick, Z. Martín-Moldes, A. Deck, R. Torres-Sanchez, A. Valat, D. Cairns, C. Li, D. L. Kaplan, *Biomaterials* **2021**, *276*, 120995; b) S. Chen, Y. Shi, X. Zhang, J. Ma, *Mater. Sci. Eng., C* **2020**, *112*, 110893.

[39] J. Li, D. J. Mooney, *Nat. Rev. Mater.* **2016**, *1*, 16071.

[40] H. Lee, M.-K. Lee, K.-H. Cheon, I.-G. Kang, C. Park, T.-S. Jang, G. Han, H.-E. Kim, J. Song, H.-D. Jung, *Mater. Des.* **2021**, *207*, 109840.